A coupled acoustic/elastic discontinuous Galerkin finite element method: Application to ultrasonic imaging of 3D-printed synthetic materials

H. Kamalinia, Andrea Barbarulo, Bing Tie

A coupled acoustic/elastic discontinuous Galerkin finite element method: application to ultrasonic imaging of 3D-printed synthetic materials

H. Kamalinia[a], A. Barbarulo[a], B. Tie[a,*]

[a] *Université Paris-Saclay, CentraleSupélec, ENS Paris-Saclay, CNRS, LMPS - Laboratoire de Mécanique Paris-Saclay, 91190, Gif-sur-Yvette, France.*

Abstract

We present the derivation of upwind numerical fluxes for the space discontinuous Galerkin (dG) finite element method applied to the numerical modeling of wave propagation in multidimensional coupled acoustic/elastic media. The space dG method is formulated using the first-order velocity-pressure and velocity-stress systems for acoustic and elastic media, respectively. After eigenanalysis of the first-order hyperbolic systems highlighting the eigenmodes of wave propagation, the upwind numerical fluxes on the acoustic/acoustic and acoustic/elastic interface are obtained in terms of exact solutions of relevant Riemann problems. Thanks to the proposed approach, explicit closed-form expressions of the upwind numerical fluxes are obtained on the acoustic/elastic interface for the general case of multidimensional anisotropic heterogeneous solid media coupled with acoustic fluids. The developed numerical fluxes are validated by analytical/numerical comparison considering the example of an acoustic domain with a circular elastic inclusion. Finally, the coupled solver is used to perform a multiparametric study on the microstructure's echogenicity in a 3D-printed synthetic material under ultrasonic imaging.

Keywords: Space discontinuous Galerkin method; Upwind numerical flux; Wave propagation; Acoustic/elastic coupling; Echogenicity.

1. Introduction

The coupled acoustic/elastic wave propagation exists in a broad range of problems, including seismic waves that interact with the outer core of the earth or the ocean, or ultrasonic waves, generated by transducers for medical imaging of patients, which propagate through human tissues and bones, and the blood inside the organs. In these problems, fluid-solid interfaces exist, and their interactions with the wave should be carefully taken into account.

An accurate numerical simulation of the acoustic and elastic wave propagation in a heterogeneous medium can be a difficult task if the characteristic size of the medium is comparable to the wavelength such that the wave interacts with the heterogeneities. This problem becomes even more challenging when dealing with multi-physics coupling. In this case, high-order methods are required to reduce the numerical dispersion and dissipation errors, and more effort is needed to maintain the high accuracy on the coupled interface [1].

Several numerical methods are introduced in the literature for solving both second-order and first-order wave equations in elastic and acoustic domains, including the acoustic/elastic interface. Di Bartolo *et al.* propose a finite difference framework with an optimized memory use based on equivalent staggered-grid schemes [2]. Among high-order finite element (FE) methods, the spectral element method is used in [3–5] to model seismic waves with different strategies of taking into account the acoustic/elastic coupling on the fluid-solid interfaces. The spatial discontinuous Galerkin (dG) is a well-established finite element method

*Corresponding author
Email address: bing.tie@centralesupelec.fr (B. Tie)

in which strategies to treat flux on element interfaces developed in the finite volume framework can be integrated, which has proven to be particularly advantageous for hyperbolic problems such as the one of elastic or acoustic wave propagation. Moreover, as the unknown fields are discontinuous from one element to another, the mass matrix is split into independent elementary matrices. Hence, the development of massively parallel solvers thus becomes straightforward [6, 7].

Unlike the continuous FE method, the space dG FE method is based on the use of discontinuous basis functions between finite elements. However, this discontinuity must be controlled by defining appropriated numerical fluxes on element interfaces. Hence, developing and implementing the appropriate numerical fluxes is essential to the success of the dG method. A rigorous and accurate numerical flux can be obtained from the exact solution of the Riemann problem on element interfaces [1, 6–11]. Otherwise, the Lax-Friedrich flux or the penalty flux is another rigorous alternative for calculating the numerical fluxes [12–18]. In the past two decades, the dG method was extensively used for numerical modeling of wave propagation in elastic media [6–9, 19–21], as well as in more complex media involving multi-physical interfaces. More particularly for the elastic-acoustic coupling, Wilcox *et al.* introduced a unified dG framework for isotropic elastic/acoustic media [1], while Zhan *et al.* considered a dG framework for arbitrary anisotropic elastic/acoustic media [10]. They all used the velocity-strain formulation and developed the upwind numerical fluxes by exactly solving the Riemann interface problem. Zhan *et al.* then extended their approach to a more general case involving poroelastic media [11]. However, unlike the present work, the method developed by Zhan *et al.* uses the velocity-strain formulation, and the numerical fluxes are developed in cartesian coordinates. Here we keep the most general coordinate-free expressions for development of the numerical fluxes. Besides, using the first-order elastic velocity-strain and acoustic velocity-pressure formulations, Ye *et al.* obtained a stable algorithm with a penalty flux defined on element interfaces [13], while Guo *et al.*, using the first-order elastic velocity-stress and acoustic velocity-pressure formulations, presented a weight-adjusted dG method also with a dissipative penalty flux defined on element interfaces [16].

This work aims to present a development of the upwind numerical fluxes in the most general case of multidimensional anisotropic elastic/acoustic media with discontinuous material properties using the wave-oriented variational framework previously proposed in [9, 21]. Within the framework of the first-order elastic velocity-stress and acoustic velocity-pressure formulations, the numerical fluxes on the interfaces, including the elastic/acoustic interfaces, are obtained in terms of the exact solution of the associated Riemann problem, unlike the penalty flux method implemented in [13]. Moreover, unlike the approach used in [10, 11], we use a coordinate-free vector and tensor notation and a wave-oriented eigenanalysis of the first-order hyperbolic system. Thanks to the proposed approach, for the general anisotropic elasticity tensor, the Riemann problem is analytically solved, and explicit closed-form expressions of the numerical fluxes in terms of wave propagation modes are obtained. These explicit expressions of fluxes are implemented in our code, and they are computed only once and stored at the beginning of each dynamic calculation.

The developed coupled acoustic/elastic solver is then employed to investigate the impact of the microstructure of 3D-printed synthetic tissues on medical ultrasonic imaging. The microstructure of biological tissues plays a crucial role in their visibility under ultrasonic imaging. At the microstructural level, biological tissues are composed of cells, extracellular matrix, and blood vessels. Each has distinct acoustic properties that can affect the echoes returned to the ultrasonic probe and the final reconstructed medical image. Recently, anatomical phantom twins are beginning to be used for surgical training and preparation for operations in some specific medical applications. These synthetic tissues created using different manufacturing techniques, including 3D-printing, are expected to mimic the acoustic properties of biological tissues in the 3-7 MHz ultrasonic imaging frequency range. The matrix of these synthetic composite materials is typically composed of a quasi-incompressible material such as elastomers or gels, closely resembling the material properties of biological tissues. The selection of different materials with different mechanical properties for the inclusions in this synthetic composite is intended to enhance the visibility of the material thickness in ultrasonic imaging by scattering the ultrasonic wave and to make the resulting image more similar to those of the biological tissue [22**?** –24].

In this work, a two-dimensional model of a 3D printed composite material containing circular inclusions is studied numerically to examine how the size and area fraction of the inclusion phase affect the ultrasonic images. The resulting ultrasonic images, called B-mode images, are obtained using a simplified model of a

sequential linear array transducer (see [25] for details).

The paper is organized as follows. In Section 2, we first present the first-order acoustic velocity-pressure formulation and then review the first-order elastic velocity-stress wave equations. An intrinsic tensorial notation is used and allows us to develop unified strong and variational frameworks [9]. Second, an analysis of the eigenstructure of the governing hyperbolic systems is given. In Section 3, the numerical flux for the acoustic/acoustic and acoustic/elastic interfaces are developed by exactly solving the relevant Riemann problem, and their explicit closed-form expressions are presented. In Section 4, the coupled acoustic/elastic dG solver using the developed upwind numerical fluxes is validated by numerical/analytical comparison considering the example of an acoustic domain with a circular elastic inclusion. Finally, in Section 5, the developed solver is applied to a 3D-printed microstructure, and virtual B-mode images of the ultrasonic wave propagation in it are reconstructed. A first parametric study on the effects of microstructural parameters on the echogenicity of the printed material is carried out.

2. Wave governing equations: strong form, variational framework, and characteristic structure

To apply the space dG FE method to the coupled acoustic/elastic wave propagation problem, the first-order hyperbolic governing equations in both elastic and acoustic media are discussed in the following sections, with the introduction of unified strong and variational frameworks for the coupled system.

2.1. First-order $\boldsymbol{v}$–p acoustic wave governing equations

Let us consider an acoustic fluid $\Omega \subset \mathbb{R}^d$ of space dimension d ($d = 1, 2, 3$) and in a time interval $[0, t_f]$. The governing equations of acoustic wave propagation in the form of a first-order velocity-pressure system can be written in the following generic form: $\forall (\boldsymbol{x}, t) \in \Omega \times]0, t_f[$

$$\boldsymbol{M}(\partial_t \boldsymbol{U}) + \boldsymbol{A}^{\partial_x}(\boldsymbol{U}) = \boldsymbol{0} \quad \text{or} \quad \begin{array}{rcl} \rho_f \partial_t \boldsymbol{v} - \boldsymbol{\nabla}_{\boldsymbol{x}} p & = & \boldsymbol{0} \\ \lambda_f^{-1} \partial_t p - \mathrm{div}_{\boldsymbol{x}} \boldsymbol{v} & = & 0 \end{array} \tag{1}$$

where the velocity and pressure fields are the primary unknowns, and ρ_f and λ_f respectively denote the density and the bulk modulus of the fluid. The tensorial compact form in (1) has been proposed by the authors in [21] within the frameworks of elastic waves. No source term is considered in the equilibrium equation without loss of generality of the purpose of the present work. The generalized unknown $\boldsymbol{U}(\boldsymbol{x}, t) = (\boldsymbol{v}(\boldsymbol{x}, t)\ p(\boldsymbol{x}, t))^T$ consists of $\boldsymbol{v}$ the velocity and p the pressure, with $(\,\cdot\,)^T$ the adjoint operator. Hence, $\boldsymbol{U}(\boldsymbol{x}, t)$ is a field in $\mathbb{R}^d \times \mathbb{R}$ and defined over the open set $\Omega \times]0, t_f[$. The operator $\boldsymbol{M}$ and space derivative operator $\boldsymbol{A}^{\partial_x}$ are defined as follows: $\forall\ \boldsymbol{W} = (\boldsymbol{w}\ q)^T$

$$\boldsymbol{M}\begin{pmatrix} \boldsymbol{w} \\ q \end{pmatrix} = \begin{pmatrix} \rho_f \boldsymbol{w} \\ \lambda_f^{-1} q \end{pmatrix},\ \boldsymbol{A}^{\partial_x}\begin{pmatrix} \boldsymbol{w} \\ q \end{pmatrix} = \begin{pmatrix} -\boldsymbol{\nabla}_{\boldsymbol{x}} q \\ -\mathrm{div}_{\boldsymbol{x}} \boldsymbol{w} \end{pmatrix} \tag{2}$$

with the usual space gradient and divergence operators $\boldsymbol{\nabla}_{\boldsymbol{x}}$ and $\mathrm{div}_{\boldsymbol{x}}$.

It is also useful to define the dot product in the vectorial space $\mathbb{R}^d \times \mathbb{R}$: $\forall\ \boldsymbol{W}_i = (\boldsymbol{w}_i\ q_i)^T, (i = 1, 2)$,

$$\boldsymbol{W}_1 \cdot \boldsymbol{W}_2 = \boldsymbol{w}_1 \cdot \boldsymbol{w}_2 + q_1 q_2 \tag{3}$$

Herein, all the vectors and tensors are denoted using bold letters.

On the boundary ∂D of any subdomain $D \subseteq \Omega$, the flux operator $\boldsymbol{F}_{\boldsymbol{n}}$ for $\boldsymbol{n} = n_i \boldsymbol{e}_i$, (herein, the Einstein summation convention is systematically used), the outward unit normal vector defined on ∂D, and associated to the first-order system (1), is: $\forall\ \boldsymbol{W} = (\boldsymbol{w}\ q)^T$,

$$\boldsymbol{F}_{\boldsymbol{n}}(\boldsymbol{W}) = \boldsymbol{A}_{\boldsymbol{n}}(\boldsymbol{W}) = \boldsymbol{A}_{\boldsymbol{n}}\begin{pmatrix} \boldsymbol{w} \\ q \end{pmatrix} = \begin{pmatrix} -q\boldsymbol{n} \\ -\boldsymbol{n} \cdot \boldsymbol{w} \end{pmatrix} \tag{4}$$

In (4), the subscript index "$\boldsymbol{n}$" indicates the dependency of $\boldsymbol{F}_{\boldsymbol{n}}$ and of $\boldsymbol{A}_{\boldsymbol{n}}$ on $\boldsymbol{n}$.

Finally, to complete the definition of the acoustic wave propagation framework, the following boundary conditions with a prescribed pressure p_D and a prescribed normal velocity v_{nN} are considered:

$$p = p_D \text{ on } \partial\Omega_D \times]0, t_f[\; ; \; \boldsymbol{v} \cdot \boldsymbol{n} = v_{nN} \text{ on } \partial\Omega_N \times]0, t_f[\tag{5}$$

with $\partial\Omega_N \cup \partial\Omega_D = \partial\Omega$ and $\partial\Omega_N \cap \partial\Omega_D = \emptyset$. On the other hand, for the initial conditions, we have:

$$p(\boldsymbol{x}, 0) = p_0(\boldsymbol{x}) \text{ and } \partial_t p(\boldsymbol{x}, 0) = \lambda_f \mathrm{div}_{\boldsymbol{x}} \boldsymbol{v}_0(\boldsymbol{x}), \;\; \forall \boldsymbol{x} \in \Omega \tag{6}$$

Remark 2.1. The first-order velocity-pressure governing equations (1) can also be written in the following equivalent form:

$$\partial_t \boldsymbol{U} + \overline{\boldsymbol{A}}^{\partial_x}(\boldsymbol{U}) = \boldsymbol{0} \;\; \text{or} \;\; \begin{array}{rcl} \partial_t \boldsymbol{v} - \rho_f^{-1} \boldsymbol{\nabla}_{\boldsymbol{x}} p &=& \boldsymbol{0} \\ \partial_t p - \lambda_f \mathrm{div}_{\boldsymbol{x}} \boldsymbol{v} &=& 0 \end{array} \tag{7}$$

with:

$$\overline{\boldsymbol{A}}^{\partial_x}\begin{pmatrix} \boldsymbol{w} \\ q \end{pmatrix} = \begin{pmatrix} -\rho_f^{-1} \boldsymbol{\nabla}_{\boldsymbol{x}} q \\ -\lambda_f \mathrm{div}_{\boldsymbol{x}} \boldsymbol{w} \end{pmatrix}, \; \overline{\boldsymbol{A}}_{\boldsymbol{n}}\begin{pmatrix} \boldsymbol{w} \\ q \end{pmatrix} = \begin{pmatrix} -\rho_f^{-1} q \boldsymbol{n} \\ -\lambda_f \boldsymbol{n} \cdot \boldsymbol{w} \end{pmatrix} = \boldsymbol{M}^{-1} \cdot \boldsymbol{A}_{\boldsymbol{n}} \tag{8}$$

The direct use of the strong form (7) leads to an inconsistent numerical flux on the physical interfaces. This issue has already been discussed in the elastic case in [9], so in-depth consideration is omitted in this paper. Hence, hereafter, the strong form (1) and the associated Jacobian operator are considered for the development of the numerical fluxes.

Remark 2.2. When applied to the first-order velocity-strain wave equations used in [1], the corresponding tensorial compact form can be written as follows for the generalized unknown $\boldsymbol{U}(\boldsymbol{x}, t) = (\boldsymbol{v}(\boldsymbol{x}, t) \; \boldsymbol{\varepsilon}(\boldsymbol{x}, t))^T$ with $\boldsymbol{\varepsilon}$ the strain field: $\forall (\boldsymbol{x}, t) \in \Omega \times]0, t_f[$,

$$\boldsymbol{M}(\partial_t \boldsymbol{U}) + \boldsymbol{A}^{\partial_x}(\boldsymbol{U}) = \boldsymbol{0} \;\; \text{or} \;\; \begin{array}{rcl} \rho_f \partial_t \boldsymbol{v} - \boldsymbol{\nabla}_{\boldsymbol{x}}(\lambda_f \mathrm{tr}(\boldsymbol{\varepsilon})) &=& \boldsymbol{0} \\ \partial_t \boldsymbol{\varepsilon} - \boldsymbol{\varepsilon}(\boldsymbol{v}) &=& \boldsymbol{0} \end{array} \tag{9}$$

with the operator $\boldsymbol{M}$ and the space derivative operator $\boldsymbol{A}^{\partial_x}$ defined as follows: $\forall \; \boldsymbol{W} = (\boldsymbol{w} \; \boldsymbol{\tau})^T$

$$\boldsymbol{M}\begin{pmatrix} \boldsymbol{w} \\ \boldsymbol{\tau} \end{pmatrix} = \begin{pmatrix} \rho_f \boldsymbol{w} \\ \boldsymbol{\tau} \end{pmatrix}, \; \boldsymbol{A}^{\partial_x}\begin{pmatrix} \boldsymbol{w} \\ \boldsymbol{\tau} \end{pmatrix} = \begin{pmatrix} -\boldsymbol{\nabla}_{\boldsymbol{x}}(\lambda_f \mathrm{tr}(\boldsymbol{\tau})) \\ -\boldsymbol{\varepsilon}(\boldsymbol{w}) \end{pmatrix} \tag{10}$$

In (9), the infinitesimal strain operator $\boldsymbol{\varepsilon}(\,\cdot\,)$ is defined as follows:

$$\boldsymbol{\varepsilon}(\boldsymbol{w}) = \frac{1}{2}\Big(\mathbf{D}_{\boldsymbol{x}} \, \boldsymbol{w} + \mathbf{D}_{\boldsymbol{x}}^T \, \boldsymbol{w}\Big) = \frac{\partial \boldsymbol{w}}{\partial x_i} \otimes_s \boldsymbol{e}_i \tag{11}$$

with "$\otimes_s$" the symmetrized tensor product defined as: $(\boldsymbol{a} \otimes_s \boldsymbol{b})_{ij} = \frac{1}{2}(a_i b_j + a_j b_i)$. Then, the flux operator $\boldsymbol{F}_{\boldsymbol{n}}$ associated to the first-order system (9) is in fact equal to $\boldsymbol{A}_{\boldsymbol{n}}$ the Jacobian operator in the $\boldsymbol{n}$ direction: $\forall \; \boldsymbol{W} = (\boldsymbol{w} \; \boldsymbol{\tau})^T$,

$$\boldsymbol{F}_{\boldsymbol{n}}(\boldsymbol{W}) = \boldsymbol{A}_{\boldsymbol{n}}(\boldsymbol{W}) = \begin{pmatrix} -\lambda_f \mathrm{tr}(\boldsymbol{\tau}) \boldsymbol{n} \\ -\boldsymbol{n} \otimes_s \boldsymbol{w} \end{pmatrix} \tag{12}$$

It is worth noticing that the method proposed in this work can be easily applied to this velocity-strain acoustic formulation.

2.2. First-order $\boldsymbol{v}$–$\boldsymbol{\sigma}$ elastic wave equations

In this section, the governing equations of elastic wave propagation previously introduced in [9, 21] is presented. We consider the wave propagation in an elastic medium $\Omega \subset \mathbb{R}^d$ of space dimension d ($d = 1, 2, 3$) and in a time interval $[0, t_f]$. The first-order velocity-stress governing equations is also written in the generic form: $\forall (\boldsymbol{x}, t) \in \Omega \times]0, t_f[$

$$\boldsymbol{M}(\partial_t \boldsymbol{U}) + \boldsymbol{A}^{\partial_x}(\boldsymbol{U}) = \boldsymbol{0} \;\; \text{or} \;\; \begin{array}{rcl} \rho \partial_t \boldsymbol{v} - \mathbf{Div}_{\boldsymbol{x}} \, \boldsymbol{\sigma} &=& \boldsymbol{0} \\ \boldsymbol{C}^{-1} : \partial_t \boldsymbol{\sigma} - \boldsymbol{\varepsilon}(\boldsymbol{v}) &=& \boldsymbol{0} \end{array} \tag{13}$$

with the following definitions of operators:

$$\boldsymbol{M}\begin{pmatrix} \boldsymbol{w} \\ \boldsymbol{\tau} \end{pmatrix} = \begin{pmatrix} \rho\boldsymbol{w} \\ \boldsymbol{C}^{-1} : \boldsymbol{\tau} \end{pmatrix}, \ \boldsymbol{A}^{\partial_x}\begin{pmatrix} \boldsymbol{w} \\ \boldsymbol{\tau} \end{pmatrix} = \begin{pmatrix} -\mathbf{Div}_{\boldsymbol{x}}\,\boldsymbol{\tau} \\ -\boldsymbol{\varepsilon}(\boldsymbol{w}) \end{pmatrix} \tag{14}$$

In (14), $\mathbf{Div}_{\boldsymbol{x}}$ denotes the usual space divergence operator of a tensor.

In the elastic case, the generalized unknown is $\boldsymbol{U}(\boldsymbol{x},t) = (\boldsymbol{v}(\boldsymbol{x},t)\ \boldsymbol{\sigma}(\boldsymbol{x},t))^T$ with $\boldsymbol{\sigma}$ the stress unknown. In (13) and (14), ρ is the density of the solid, $\boldsymbol{C}$ the fourth-order elasticity tensor, and ":" the usual double-dot product between two tensors defined as $(\boldsymbol{C} : \boldsymbol{\tau})_{ij} = C_{ijkl}\tau_{kl}$.

Similar to the acoustic wave framework, it is useful to define the dot product this time in the vectorial space of $\mathbb{R}^d \times \mathbb{R}^{d\times d_{sym}}$: $\forall\ \boldsymbol{W}_i = (\boldsymbol{w}_i\ \boldsymbol{\tau}_i)^T, (i = 1, 2)$,

$$\boldsymbol{W}_1 \cdot \boldsymbol{W}_2 = \boldsymbol{w}_1 \cdot \boldsymbol{w}_2 + \boldsymbol{\tau}_1 : \boldsymbol{\tau}_2 \tag{15}$$

The flux operator $\boldsymbol{F}_{\boldsymbol{n}}$ on the boundary ∂D of any subdomain $D \subseteq \Omega$ is defined as: $\forall\ \boldsymbol{W} = (\boldsymbol{w}\ \boldsymbol{\tau})^T$,

$$\boldsymbol{F}_{\boldsymbol{n}}(\boldsymbol{W}) = \boldsymbol{A}_{\boldsymbol{n}}(\boldsymbol{W}) = \begin{pmatrix} -\boldsymbol{\tau}\cdot\boldsymbol{n} \\ -\boldsymbol{n}\otimes_s \boldsymbol{w} \end{pmatrix} \tag{16}$$

2.3. dG variational framework

Now that all the required operators and parameters are defined, the unified variational framework can be introduced. Within the framework of the discontinuous Galerkin FE method, we look for an approximated solution $\boldsymbol{U}_h$, discontinuous across the element interfaces, of the generalized unknown $\boldsymbol{U}$. This discontinuous character of $\boldsymbol{U}_h$ makes it possible to integrate the concept of well-established numerical fluxes within the framework of the finite volume method [6].

Let us consider $\mathscr{M}_h = \{\Omega_k\}_k$ a FE mesh of the domain Ω. For the sake of simplicity, from now on, any element Ω_k of the mesh $\mathscr{M}_h$ will be denoted by E and any of the neighboring elements of E by E'. To obtain the dG variational formulation of the coupled acoustic/elastic system (1) and (13) for any element E, the integration by parts formula is used, and the discontinuous flux $\boldsymbol{F}_n(\boldsymbol{U}_h)$ on the element boundary ∂E is replaced by a numerical flux $\hat{\boldsymbol{F}}_{\boldsymbol{n}}(\boldsymbol{U}_h, \boldsymbol{U}'_h)$, which depends on the solution in both E and the adjacent element E'. Then we get: $\forall\ \boldsymbol{W}_h(\boldsymbol{x})$,

$$(\boldsymbol{W}_h, \boldsymbol{M}(\partial_t \boldsymbol{U}_h))_E - (\boldsymbol{A}^{\partial_x,T}(\boldsymbol{W}_h), \boldsymbol{U}_h)_E + < \boldsymbol{W}_h, \hat{\boldsymbol{F}}_{\boldsymbol{n}}(\boldsymbol{U}_h, \boldsymbol{U}'_h) >_{\partial E} = 0 \tag{17}$$

where $\boldsymbol{U}_h$ and $\boldsymbol{U}'_h$ are elementary solutions in E and E', respectively, and $\boldsymbol{U}_h \neq \boldsymbol{U}'_h$ on $\partial E \cap \partial E'$. $\boldsymbol{W}_h(\boldsymbol{x})$ are test functions, with $\boldsymbol{W}_h(\boldsymbol{x}) = (\boldsymbol{w}_h(\boldsymbol{x})\ q_h(\boldsymbol{x}))^T$ in the acoustic case and $\boldsymbol{W}_h(\boldsymbol{x}) = (\boldsymbol{w}_h(\boldsymbol{x})\ \boldsymbol{\tau}_h(\boldsymbol{x}))^T$ in the elastic case. In (17), following notations are adopted for volume and surface integrations, respectively:

$$(\boldsymbol{W}_1, \boldsymbol{W}_2)_E = \int_E \boldsymbol{W}_1 \cdot \boldsymbol{W}_2 \,\mathrm{d}V\ , \ < \boldsymbol{W}_1, \boldsymbol{W}_2 >_{\partial E} = \int_{\partial E} \boldsymbol{W}_1 \cdot \boldsymbol{W}_2 \,\mathrm{d}S \tag{18}$$

Applying integration by parts again to (17) leads to the following equivalent form of (17): $\forall\ \boldsymbol{W}_h(\boldsymbol{x})$,

$$(\boldsymbol{W}_h, \boldsymbol{M}(\partial_t \boldsymbol{U}_h))_E + (\boldsymbol{W}_h, \boldsymbol{A}^{\partial_x}(\boldsymbol{U}_h))_E + < \boldsymbol{W}_h, \hat{\boldsymbol{F}}_{\boldsymbol{n}}(\boldsymbol{U}_h, \boldsymbol{U}'_h) - \boldsymbol{F}(\boldsymbol{U}_h) >_{\partial E} = 0 \tag{19}$$

It is this variational formulation (19) that is used in the present work to implement the dG solver because it involves the slightly more familiar operator $\boldsymbol{A}^{\partial_x}$, instead of $\boldsymbol{A}^{\partial_x,T}$.

The study of the numerical fluxes on internal element boundaries $\partial E_{int} = \partial E \backslash (\partial E \cap \partial\Omega)$ is presented in Section 3. For external element boundaries $\partial E_{ext} = \partial E \cap \partial\Omega$, a ghost neighbor element E' with the same mechanical behavior as E is assumed [20]. In the case of an acoustic medium, one should prescribe $p'_h = 2p_D - p_h$ and $\boldsymbol{v}'_h \cdot \boldsymbol{n} = \boldsymbol{v}_h \cdot \boldsymbol{n}$ on $\partial E \cap \partial\Omega_D$, and $p'_h = p_h$ and $\boldsymbol{v}'_h \cdot \boldsymbol{n} = 2v_{nN} - \boldsymbol{v}_h \cdot \boldsymbol{n}$ on $\partial E \cap \partial\Omega_N$. The same approach is considered for the elastic external element boundary elaborated in [9].

2.4. Characteristic structure of the wave governing equations

Before giving the definition of Riemann problems on element interfaces in the next section, it is necessary to analyze the characteristic structure of the wave equations (1) and (13) for both acoustic and elastic cases. To do this, we analyze the corresponding eigenvalue problem defined with the operator $\boldsymbol{M}$ and the Jacobian operator $\boldsymbol{A_n}$ as follows

$$\boldsymbol{A_n}(\boldsymbol{R_n}) = \lambda_{\boldsymbol{n}} \boldsymbol{M}(\boldsymbol{R_n}) \tag{20}$$

2.4.1. Eigenanalysis of the acoustic wave equation

In the acoustic case, we get $m = d + 1$ eigenvalues $\{\lambda_{\boldsymbol{n},k}\}_{k=1,...m}$ and m associated right eigenvectors $\{\boldsymbol{R_{n},k}\}_{k=1,...m}$ from (20). It is noteworthy that the associated eigenvalue and eigenvectors of the two equivalent forms of the governing equations (1) and (7) are identical. In other words, one can use (8) to rewrite the eigenproblem (20) in the following form:

$$\overline{\boldsymbol{A}}_{\boldsymbol{n}}(\boldsymbol{R_n}) = \lambda_{\boldsymbol{n}} \boldsymbol{R_n} \tag{21}$$

Solving (21) results in two nonzero eigenvalues and the associated right eigenvectors:

$$\lambda_{\boldsymbol{n}}^{\pm} = \pm\sqrt{\frac{\lambda_f}{\rho_f}}\ ,\ \boldsymbol{R_n^{\pm}} = \begin{pmatrix} \frac{1}{\sqrt{2}}\boldsymbol{n} \\ -\frac{1}{\sqrt{2}}\lambda_f(\lambda_{\boldsymbol{n}}^{\pm})^{-1} \end{pmatrix} = \begin{pmatrix} \frac{1}{\sqrt{2}}\boldsymbol{n} \\ -\frac{1}{\sqrt{2}}z_{\boldsymbol{n}}^{\pm} \end{pmatrix} \tag{22}$$

where $z_{\boldsymbol{n}}$ is the acoustic impedance defined as $z_{\boldsymbol{n}}^{\pm} = \lambda_f(\lambda_{\boldsymbol{n}}^{\pm})^{-1} = \rho_f \lambda_{\boldsymbol{n}}^{\pm}$.

For the calculation of the left eigenvectors of (21), which are also the right eigenvectors of the tensor $\overline{\boldsymbol{A}}_{\boldsymbol{n}}^T$ defined as:

$$\overline{\boldsymbol{A}}_{\boldsymbol{n}}^T(\boldsymbol{W}) = \begin{pmatrix} -\lambda_f q\boldsymbol{n} \\ -\rho_f^{-1}\boldsymbol{n}\cdot\boldsymbol{w} \end{pmatrix} \tag{23}$$

It can be shown that:

$$\boldsymbol{L_n^{\pm}} = \begin{pmatrix} \frac{1}{\sqrt{2}}\boldsymbol{n} \\ -\frac{1}{\sqrt{2}}(z_{\boldsymbol{n}}^{\pm})^{-1} \end{pmatrix}\ ,\ \boldsymbol{M}(\boldsymbol{R_n^{\pm}}) = \rho_f \boldsymbol{L_n^{\pm}} \tag{24}$$

Hence, we get the following decompositions of the flux (or jacobian) tensors:

$$\overline{\boldsymbol{A}}_{\boldsymbol{n}} = \lambda_{\boldsymbol{n}}^{\pm}\boldsymbol{R_n^{\pm}} \otimes \boldsymbol{L_n^{\pm}}\ ,\ \boldsymbol{A_n} = z_{\boldsymbol{n}}^{\pm}\boldsymbol{L_n^{\pm}} \otimes \boldsymbol{L_n^{\pm}} \tag{25}$$

The systeme (20) is therefore symmetric and has $\boldsymbol{R_n^{\pm}}$ as eigenvectors.

2.4.2. Eigenanalysis of the elastic wave equation

The characteristic structure of the first-order hyperbolic velocity-stress equation (13) is studied in [21]. Here, some of the important results are recalled.

Among the $m = d + d(d+1)/2$ eigenvalues of $\boldsymbol{A_n}$, there are d strictly negative eigenvalues and d strictly positive eigenvalues, representing the propagation speed of quasi-longitudinal "qL" and quasi transverse "qT" wave modes propagating in the $\boldsymbol{n}$ direction. The right and left eigenmodes corresponding to the nonzero eigenvalues of $\overline{\boldsymbol{A}}_{\boldsymbol{n}} = \boldsymbol{M}^{-1}\cdot\boldsymbol{A_n}$ are the following: $\forall k = qL, \{qT_\alpha\}_{\alpha=1,\cdots,d-1}$

$$\boldsymbol{R_{n,k}^{\pm}} = \begin{pmatrix} \boldsymbol{w_{n,k}} \\ -\rho(z_{\boldsymbol{n},k}^{\pm})^{-1}\boldsymbol{C} : (\boldsymbol{n} \otimes_s \boldsymbol{w_{n,k}}) \end{pmatrix}\ ,\ \boldsymbol{L_{n,k}^{\pm}} = \begin{pmatrix} \boldsymbol{w_{n,k}} \\ -(z_{\boldsymbol{n},k}^{\pm})^{-1}\boldsymbol{n} \otimes_s \boldsymbol{w_{n,k}} \end{pmatrix} \tag{26}$$

where $z_{\boldsymbol{n},k}^{\pm} = \rho\lambda_{\boldsymbol{n},k}^{\pm}$ denotes the acoustic impedance of kth eigenmode and $\boldsymbol{w_{n,k}} = \frac{1}{\sqrt{2}}\boldsymbol{\gamma_{n,k}}$ with $\boldsymbol{\gamma_{n,k}}$ unit eigenvectors of $\boldsymbol{\Gamma_n}$ the Christoffel tensor:

$$\boldsymbol{\Gamma_n}\cdot\boldsymbol{\gamma_{n,k}} = \lambda_{\boldsymbol{n},k}^2\boldsymbol{\gamma_{n,k}},\ \ k = qL, \{qT_\alpha\}_{\alpha=1,\cdots,d-1} \tag{27}$$

and $\boldsymbol{\Gamma_n}$ is defined as:

$$\boldsymbol{\Gamma_n}\cdot\boldsymbol{w} = \left(\rho^{-1}\boldsymbol{C} : (\boldsymbol{n} \otimes_s \boldsymbol{w_{n,k}})\right)\cdot\boldsymbol{n}, \forall\boldsymbol{w} \tag{28}$$

Finally, as in the acoustic case, the following equations hold:

$$\boldsymbol{M}(\boldsymbol{R_{n,k}^{\pm}}) = \rho\boldsymbol{L_{n,k}^{\pm}}\ ,\ \boldsymbol{A_n} = z_{\boldsymbol{n},k}^{\pm}\boldsymbol{L_{n,k}^{\pm}} \otimes \boldsymbol{L_{n,k}^{\pm}} \tag{29}$$

3. Upwind numerical fluxes

This section develops upwind numerical fluxes for multidimensional coupled anisotropic elastic-acoustic wave equations with discontinuous material properties (*i.e.*, media including physical interfaces), more particularly, those for acoustic-acoustic and acoustic-elastic interfaces. Upwind numerical fluxes for elastic-elastic interfaces for heterogeneous anisotropic solids have been studied in detail in [9, 21]. The acoustic-acoustic case is simple and has already been treated in the literature. Still, for the sake of completeness, it is considered below in order to have the numerical fluxes expressed with the same notations used in the present work. Our main contribution is the development of numeric fluxes on acoustic/elastic interfaces.

3.1. Numerical fluxes across an acoustic-acoustic interface

We consider the interface of two adjacent elements E and E', governed by the previously presented velocity-pressure acoustic wave equations and having respectively $(\rho_f, \lambda_f, \boldsymbol{U}_h)$ and $(\rho'_f, \lambda'_f, \boldsymbol{U}'_h)$ as densities, bulk modulus and initial states (Figure 1). The Riemann problem defines the states that result from the discontinuity $(\boldsymbol{U}_h - \boldsymbol{U}'_h)$'s propagation. All the following equations are written in the 3D case without loss of generality.

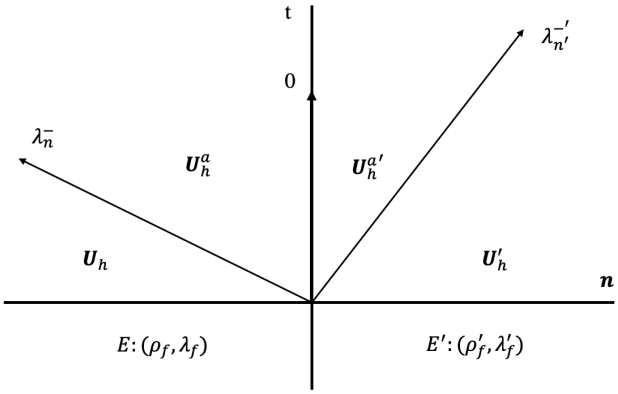

Figure 1. Sketch illustration of the Rankine-Hugoniot jump condition in the Riemann problem at an acoustic-acoustic element interface

$$\boldsymbol{A}_{\boldsymbol{n}}(\boldsymbol{U}_h - \boldsymbol{U}_h^a) = \lambda_{\boldsymbol{n}}^- \boldsymbol{M}(\boldsymbol{U}_h - \boldsymbol{U}_h^a) \tag{30a}$$

$$\boldsymbol{A}_{\boldsymbol{n}}(\boldsymbol{U}_h^a) + \boldsymbol{A}'_{\boldsymbol{n}'}(\boldsymbol{U}_h^{a'}) = \boldsymbol{0} \tag{30b}$$

$$\boldsymbol{A}'_{\boldsymbol{n}'}(\boldsymbol{U}'_h - \boldsymbol{U}_h^{a'}) = \lambda_{\boldsymbol{n}'}^{-'} \boldsymbol{M}'(\boldsymbol{U}'_h - \boldsymbol{U}_h^{a'}) \tag{30c}$$

We note that the two outward unit normal vectors $\boldsymbol{n}$ and $\boldsymbol{n}'$ of E and E' on their interface verify $\boldsymbol{n} + \boldsymbol{n}' = \boldsymbol{0}$. According to the definition of the eigenvalues and eigenvectors (20), the discontinuity terms in (30) can be decomposed as follows within the right eigenvectors basis:

$$\boldsymbol{U}_h - \boldsymbol{U}_h^a = \alpha \boldsymbol{R}_{\boldsymbol{n}}^- \ , \ \boldsymbol{U}'_h - \boldsymbol{U}_h^{a'} = \alpha' \boldsymbol{R}_{\boldsymbol{n}'}^{-'} \tag{31}$$

By applying (31) and the second identity of (24), the Rankine–Hugoniot jump conditions (30) finally become:

$$\boldsymbol{A}_{\boldsymbol{n}}(\boldsymbol{U}_h) - \boldsymbol{A}_{\boldsymbol{n}}(\boldsymbol{U}_h^a) = \alpha z_{\boldsymbol{n}}^- \boldsymbol{L}_{\boldsymbol{n}}^- \tag{32a}$$

$$\boldsymbol{A}_{\boldsymbol{n}}(\boldsymbol{U}_h^a) + \boldsymbol{A}'_{\boldsymbol{n}'}(\boldsymbol{U}_h^{a'}) = \boldsymbol{0} \tag{32b}$$

$$\boldsymbol{A}'_{\boldsymbol{n}'}(\boldsymbol{U}'_h) - \boldsymbol{A}'_{\boldsymbol{n}'}(\boldsymbol{U}_h^{a'}) = \alpha' z_{\boldsymbol{n}'}^{-'} \boldsymbol{L}_{\boldsymbol{n}'}^{-'} \tag{32c}$$

It is worth noting that, according to the definition of the Jacobian operator (8), the equation (32b) corresponds to the following classical interface conditions for perfect fluids:

$$p_h^a - p_h^{a'} = 0 \ , \ \boldsymbol{v}_h^a \cdot \boldsymbol{n} + \boldsymbol{v}_h^{a'} \cdot \boldsymbol{n}' = 0 \tag{33}$$

Solving the Riemann problem (32) leads to the determination of the two unknown states $\{\boldsymbol{U}^a, \boldsymbol{U}^{a'}\}$, *i.e.*, the two characteristic coefficients $\{\alpha, \alpha'\}$. By eliminating the two unknown states $\boldsymbol{U}_h^a$ and $\boldsymbol{U}_h^{a'}$ in (32) and using (33), the Riemann problem (32) is solved, we obtain the following formulas for $\{\alpha, \alpha'\}$ (see Appendix A1):

$$\alpha = \tilde{\boldsymbol{L}}_{\boldsymbol{n}}^- \cdot (\boldsymbol{U}_h - \boldsymbol{U}_h') \ , \ \alpha' = \tilde{\boldsymbol{L}}_{\boldsymbol{n}'}^{-'} \cdot (\boldsymbol{U}_h' - \boldsymbol{U}_h) \tag{34}$$

In (34), the two "perturbed" left eigenmodes $\{\tilde{\boldsymbol{L}}_{\boldsymbol{n},k}^-, \tilde{\boldsymbol{L}}_{\boldsymbol{n}',k}^{-'}\}$ are calculated as follows and couple the material properties of the adjacent elements E and E':

$$\tilde{\boldsymbol{L}}_{\boldsymbol{n}}^- = \begin{pmatrix} C_z^- \wp_{vect}(\boldsymbol{L}_{\boldsymbol{n}}^-) \\ C_z^{-'} \wp_{scalar}(\boldsymbol{L}_{\boldsymbol{n}}^-) \end{pmatrix} \ , \ \tilde{\boldsymbol{L}}_{\boldsymbol{n}'}^{-'} = \begin{pmatrix} C_z^{-'} \wp_{vect}(\boldsymbol{L}_{\boldsymbol{n}'}^{-'}) \\ C_z^- \wp_{scalar}(\boldsymbol{L}_{\boldsymbol{n}'}^{-'}) \end{pmatrix} \tag{35}$$

with:

$$C_z^- = \frac{\overline{z_{\boldsymbol{n}}^-}^R}{z_{\boldsymbol{n}}^-} = \frac{z_{\boldsymbol{n}}^{-'}}{\overline{z_{\boldsymbol{n}}^-}^V} > 0 \ , \ C_z^{-'} = \frac{\overline{z_{\boldsymbol{n}}^-}^R}{z_{\boldsymbol{n}'}^{-'}} = \frac{z_{\boldsymbol{n}}^-}{\overline{z_{\boldsymbol{n}}^-}^V} > 0 \tag{36}$$

$\overline{z_{\boldsymbol{n}}^-}^R$ and $\overline{z_{\boldsymbol{n}}^-}^V$ respectively denote the harmonic and arithmetic means, between E and E', of the acoustic impedance of the eigenvector. Furthermore, two operators $\wp_{vect}(\,\cdot\,)$ and $\wp_{scalar}(\,\cdot\,)$ are introduced to treat the vectorial and scalar part of a generalized field $\boldsymbol{W} = (\boldsymbol{w}\ q)^T$ separately, and they are defined as follows:

$$\wp_{vect}(\boldsymbol{W}) = \boldsymbol{w} \ , \ \wp_{scalar}(\boldsymbol{W}) = q \tag{37}$$

Finally, the upwind numerical fluxes defined as $\hat{\boldsymbol{F}}_{\boldsymbol{n}}(\boldsymbol{U}_h, \boldsymbol{U}_h') = \boldsymbol{A}_{\boldsymbol{n}}(\boldsymbol{U}_h^a) = \frac{1}{2}(\boldsymbol{A}_{\boldsymbol{n}}(\boldsymbol{U}_h^a) - \boldsymbol{A}_{\boldsymbol{n}'}'(\boldsymbol{U}_h^{a'}))$ can be calculated by replacing the calculated characteristic coefficients in following equivalent equations:

$$\hat{\boldsymbol{F}}_{\boldsymbol{n}}(\boldsymbol{U}_h, \boldsymbol{U}_h') = \frac{1}{2}\big(\boldsymbol{A}_{\boldsymbol{n}}(\boldsymbol{U}_h) - \boldsymbol{A}_{\boldsymbol{n}'}'(\boldsymbol{U}_h') - \alpha z_{\boldsymbol{n}}^- \boldsymbol{L}_{\boldsymbol{n}}^- + \alpha' z_{\boldsymbol{n}'}^{-'} \boldsymbol{L}_{\boldsymbol{n}'}^{-'}\big) \tag{38a}$$

$$= \boldsymbol{A}_{\boldsymbol{n}}(\boldsymbol{U}_h) - \alpha z_{\boldsymbol{n}}^- \boldsymbol{L}_{\boldsymbol{n}}^- \tag{38b}$$

3.2. Numerical fluxes across an acoustic-elastic interface

We again consider the interface of two adjacent elements E and E'. But now, the element E is governed by the acoustic wave equations with $(\rho_f, \lambda_f, \boldsymbol{U}_h)$ as density, bulk modulus, and initial state, and E' is governed by the elastic wave equations with $(\rho', C', \boldsymbol{U}_h')$ as density, elasticity tensor, and initial state (Figure 2). In this case, the Rankine-Hugoniot jump conditions are written as follows:

$$\boldsymbol{A}_{\boldsymbol{n}}(\boldsymbol{U}_h - \boldsymbol{U}_h^a) = \lambda_{\boldsymbol{n}}^- \boldsymbol{M}(\boldsymbol{U}_h - \boldsymbol{U}_h^a) \tag{39a}$$

$$\boldsymbol{A}_{\boldsymbol{n}}(\boldsymbol{U}_h^a) + \boldsymbol{\Pi}_{\boldsymbol{n}'}(\boldsymbol{A}_{\boldsymbol{n}'}'(\boldsymbol{U}_h^{c'})) = \boldsymbol{0} \tag{39b}$$

$$\boldsymbol{A}_{\boldsymbol{n}'}'(\boldsymbol{U}_h^{b'} - \boldsymbol{U}_h^{c'}) = \lambda_{\boldsymbol{n}',qT_2}^{-'} \boldsymbol{M}'(\boldsymbol{U}_h^{b'} - \boldsymbol{U}_h^{c'}) \tag{39c}$$

$$\boldsymbol{A}_{\boldsymbol{n}'}'(\boldsymbol{U}_h^{a'} - \boldsymbol{U}_h^{b'}) = \lambda_{\boldsymbol{n}',qT_1}^{-'} \boldsymbol{M}'(\boldsymbol{U}_h^{a'} - \boldsymbol{U}_h^{b'}) \tag{39d}$$

$$\boldsymbol{A}_{\boldsymbol{n}'}'(\boldsymbol{U}_h' - \boldsymbol{U}_h^{a'}) = \lambda_{\boldsymbol{n},qL}^{-'} \boldsymbol{M}'(\boldsymbol{U}_h' - \boldsymbol{U}_h^{a'}) \tag{39e}$$

In (39), the operator $\boldsymbol{\Pi}_{\boldsymbol{n}'}$ from $\mathbb{R}^d \times \mathbb{R}^{d \times d_{sym}}$ to $\mathbb{R}^d \times \mathbb{R}$ is defined as follows: $\forall \boldsymbol{W} = (\boldsymbol{w}\ \boldsymbol{\tau})^T \in \mathbb{R}^d \times \mathbb{R}^{d \times d_{sym}}$,

$$\boldsymbol{\Pi}_{\boldsymbol{n}'}(\boldsymbol{W}) = \begin{pmatrix} \boldsymbol{w} \\ (\boldsymbol{n}' \otimes \boldsymbol{n}') : \boldsymbol{\tau} \end{pmatrix} \tag{40}$$

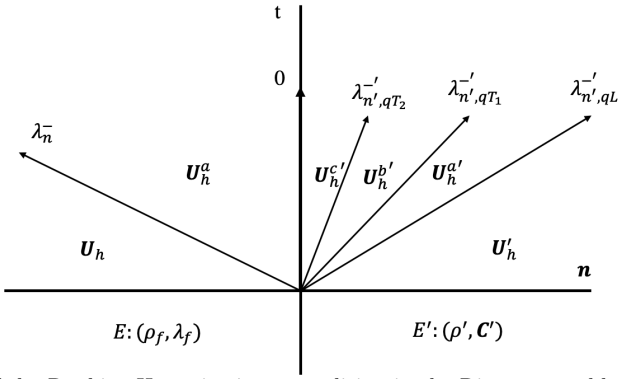

Figure 2. Sketch illustration of the Rankine-Hugoniot jump condition in the Riemann problem at an acoustic-elastic element interface

Then, it can be shown that according to the definition of $\boldsymbol{A_n}$ in both acoustic and elastic media and the definition of $\boldsymbol{\Pi}_{\boldsymbol{n}'}$, the equation (39b) corresponds to the following classical perfect fluid-solid interface conditions:

$$p^a_h \boldsymbol{n} + \boldsymbol{\sigma}^{c'}_h \cdot \boldsymbol{n}' = \boldsymbol{0} \ , \ \boldsymbol{n} \cdot \boldsymbol{v}^a_h + \boldsymbol{n}' \cdot \boldsymbol{v}^{c'}_h = 0 \tag{41}$$

Now, as in the acoustic-acoustic case, the discontinuity terms in (39) are decomposed as follows using the right eigenvectors basis:

$$\boldsymbol{U}_h - \boldsymbol{U}^a_h = \alpha \boldsymbol{R}^-_{\boldsymbol{n}} \tag{42a}$$

$$\boldsymbol{U}'_h - \boldsymbol{U}^{a'}_h = \alpha'_{qL} \boldsymbol{R}^{-'}_{\boldsymbol{n}',qL}, \ \ \boldsymbol{U}^{a'}_h - \boldsymbol{U}^{b'}_h = \alpha'_{qT_1} \boldsymbol{R}^{-'}_{\boldsymbol{n}',qT_1}, \ \ \boldsymbol{U}^{b'}_h - \boldsymbol{U}^{c'}_h = \alpha'_{qT_2} \boldsymbol{R}^{-'}_{\boldsymbol{n}',qT_2} \tag{42b}$$

By adding the three last equations given by (39c)–(39e), and by applying (42), the second identity of (24), and the first identity of (29), the Rankine–Hugoniot jump conditions (39) finally become:

$$\boldsymbol{A_n}(\boldsymbol{U}_h) - \boldsymbol{A_n}(\boldsymbol{U}^a_h) = \alpha z^-_{\boldsymbol{n}} \boldsymbol{L}^-_{\boldsymbol{n}} \tag{43a}$$

$$\boldsymbol{A_n}(\boldsymbol{U}^a_h) + \boldsymbol{\Pi}_{\boldsymbol{n}'}(\boldsymbol{A}'_{\boldsymbol{n}'}(\boldsymbol{U}^{c'}_h)) = \boldsymbol{0} \tag{43b}$$

$$\boldsymbol{A}'_{\boldsymbol{n}'}(\boldsymbol{U}'_h) - \boldsymbol{A}'_{\boldsymbol{n}'}(\boldsymbol{U}^{c'}_h) = \alpha'_k z^{-'}_{\boldsymbol{n}',k} \boldsymbol{L}^{-'}_{\boldsymbol{n}',k} \tag{43c}$$

Again by eliminating the two unknown states $\boldsymbol{U}^a_h$ and $\boldsymbol{U}^{c'}_h$ in (43), it can be shown that the characteristic coefficients $\{\alpha, \alpha'_k\}$ of the Riemann problem (43) are solutions of the following linear system of equations (see Appendix A2):

$$\begin{bmatrix} 1 & [B^{ae}]_{1\times 3} \\ [B^{ae'}]_{3\times 1} & [Id]_{3\times 3} \end{bmatrix} \cdot \begin{pmatrix} \alpha \\ \{\alpha'_k\} \end{pmatrix} = \begin{bmatrix} \boldsymbol{L}^-_{\boldsymbol{n}} \cdot (\boldsymbol{U}_h - \boldsymbol{\Pi}_{\boldsymbol{n}'}(\boldsymbol{U}'_h)) \\ \{2 \wp_{tens}(\boldsymbol{L}^{-'}_{\boldsymbol{n}',k}) : \wp_{tens}(\boldsymbol{U}'_h - \boldsymbol{\Psi}_{\boldsymbol{n}}(\boldsymbol{U}_h))\} \end{bmatrix} \tag{44}$$

where the components of the matrices $[B^{ae}]$ and $[B^{ae'}]$ are:

$$B^{ae}_{1k} = -\frac{z^-_{\boldsymbol{n}} - z^{-'}_{\boldsymbol{n}',k}}{2 z^-_{\boldsymbol{n}}} \boldsymbol{n} \cdot \boldsymbol{\gamma}'_{\boldsymbol{n}',k} \ , \ B^{ae'}_{k1} = \frac{z^-_{\boldsymbol{n}}}{z^{-'}_{\boldsymbol{n}',k}} \boldsymbol{n} \cdot \boldsymbol{\gamma}'_{\boldsymbol{n}',k} \tag{45}$$

in (44), the operator $\boldsymbol{\Psi}_{\boldsymbol{n}}$ from $\mathbb{R}^d \times \mathbb{R}$ to $\mathbb{R}^d \times \mathbb{R}^{d \times d_{sym}}$ is defined as follows: $\forall \boldsymbol{W} = (\boldsymbol{w} \ q)^T \in \mathbb{R}^d \times \mathbb{R}$,

$$\boldsymbol{\Psi}_{\boldsymbol{n}}(\boldsymbol{W}) = \begin{pmatrix} \boldsymbol{w} \\ q \boldsymbol{n} \otimes \boldsymbol{n} \end{pmatrix} \tag{46}$$

After solving the system of equations (44), one finally gets:

$$\alpha = D^{ae}_{11} \boldsymbol{L}^-_{\boldsymbol{n}} \cdot (\boldsymbol{U}_h - \boldsymbol{\Pi}_{\boldsymbol{n}'}(\boldsymbol{U}'_h)) - 2 H^{ae}_{1k} \wp_{tens}(\boldsymbol{L}^{-'}_{\boldsymbol{n}',k}) : \wp_{tens}(\boldsymbol{U}'_h - \boldsymbol{\Psi}_{\boldsymbol{n}}(\boldsymbol{U}_h)) \tag{47}$$

with D_{11}^{ae} and H_{1k}^{ae} defined by:

$$[R^{ae}]^{-1} = \begin{bmatrix} 1 & [B^{ae}]_{1\times 3} \\ [B^{ae'}]_{3\times 1} & [Id]_{3\times 3} \end{bmatrix}^{-1} = \begin{bmatrix} D_{11}^{ae} & -[H^{ae}]_{1\times 3} \\ -[H^{ae'}]_{3\times 1} & [D^{ae'}]_{3\times 3} \end{bmatrix} \tag{48}$$

Then, the numerical flux is calculated within the acoustic element E using the equation (38b).

When the elastic element E' is isotropic, we get one pure longitudinal "L" mode and two pure transverse "T" modes, i.e.,:

$$\boldsymbol{n}\cdot\boldsymbol{\gamma}'_{\boldsymbol{n}',L} = 0 \ , \ \boldsymbol{n}\cdot\boldsymbol{\gamma}'_{\boldsymbol{n}',T_1} = \boldsymbol{n}\cdot\boldsymbol{\gamma}'_{\boldsymbol{n}',T_2} = 0 \tag{49}$$

According to (44)-(45), α, the acoustic wave in E, is only coupled to α'_L, the elastic longitudinal wave in E', which is a well-known classical result. Otherwise, the quasi-transverse elastic waves are always coupled to the acoustic wave through an acoustic-elastic interface.

Remark 3.1 For the case in which E is governed by elastic wave equations and the neighboring E' is governed by acoustic wave equations, by reversing the role of E and E' in the preceding equations (39), (42) and (43), after calculation of the characteristic coefficients $\{\{\alpha_k\},\alpha'\}$, the characteristic coefficients $\{\alpha,\alpha'_k\}$ of the Riemann problem (43) are solutions of the following linear system of equations (see Appendix A2):

$$\begin{bmatrix} [Id]_{3\times 3} & [B^{ea}]_{3\times 1} \\ [B^{ea'}]_{1\times 3} & 1 \end{bmatrix} \cdot \begin{pmatrix} \{\alpha_k\} \\ \alpha' \end{pmatrix} = \begin{bmatrix} \{2\wp_{tens}(\boldsymbol{L}^-_{\boldsymbol{n},k}) : \wp_{tens}(\boldsymbol{U}_h - \boldsymbol{\Psi}_{\boldsymbol{n}'}(\boldsymbol{U}'_h))\} \\ \boldsymbol{L}^{-'}_{\boldsymbol{n}'} \cdot (\boldsymbol{\Pi}_{\boldsymbol{n}}(\boldsymbol{U}_h) - \boldsymbol{U}'_h) \end{bmatrix} \tag{50}$$

where the components of the matrices $[B^{ea}]$ and $[B^{ea'}]$ are:

$$B_{k1}^{ea} = \frac{z^{-'}_{\boldsymbol{n}'}}{z^-_{\boldsymbol{n},k}}\boldsymbol{n}'\cdot\boldsymbol{\gamma}_{\boldsymbol{n},k} \ , \ B_{1k}^{ea'} = -\frac{z^-_{\boldsymbol{n},k} - z^{-'}_{\boldsymbol{n}'}}{2z^{-'}_{\boldsymbol{n}'}}\boldsymbol{n}'\cdot\boldsymbol{\gamma}_{\boldsymbol{n},k} \tag{51}$$

After solving the system of equations (50) for characteristic equations, one finally gets:

$$\alpha_k = 2D_{kl}^{ea}\wp_{tens}(\boldsymbol{L}^-_{\boldsymbol{n},l})) : \wp_{tens}(\boldsymbol{U}_h - \boldsymbol{\Psi}_{\boldsymbol{n}'}(\boldsymbol{U}'_h)) - H_{k1}^{ea}\boldsymbol{L}^{-'}_{\boldsymbol{n}'}\cdot(\boldsymbol{\Pi}_{\boldsymbol{n}}(\boldsymbol{U}_h) - \boldsymbol{U}'_h) \tag{52}$$

with D_{kl}^{ea} and H_{k1}^{ea} defined by:

$$[R^{ea}]^{-1} = \begin{bmatrix} [Id]_{3\times 3} & [B^{ea}]_{3\times 1} \\ [B^{ea'}]_{1\times 3} & 1 \end{bmatrix}^{-1} = \begin{bmatrix} [D^{ea}]_{3\times 3} & -[H^{ea}]_{3\times 1} \\ -[H^{ea'}]_{1\times 3} & D_{11}^{ea'} \end{bmatrix} \tag{53}$$

Then, the numerical flux is calculated within the elastic element E using the following equation [9]:

$$\hat{\boldsymbol{F}}_{\boldsymbol{n}}(\boldsymbol{U}_h,\boldsymbol{U}'_h) = \boldsymbol{A}_{\boldsymbol{n}}(\boldsymbol{U}_h) - \alpha_k z^-_{\boldsymbol{n},k}\boldsymbol{L}^-_{\boldsymbol{n},k} \tag{54}$$

3.3. Implementation and calculation of numerical fluxes in the variational formulation

For an acoustic-elastic interface, we briefly present how to implement and compute the terms associated with the numerical fluxes in the variational formulation (19).

Let us consider first the acoustic element, denoted E. In this case, the interface is consequently denoted ∂E^{ae} and the elastic element E'. Taking into account (38b) and (47), The flux term in (19) becomes:

$$\begin{aligned} & < \boldsymbol{W}_h, \hat{\boldsymbol{F}}_{\boldsymbol{n}}(\boldsymbol{U}_h,\boldsymbol{U}'_h) - \boldsymbol{F}(\boldsymbol{U}_h) >_{\partial E^{ae}} \\ =& - < \boldsymbol{W}_h, \alpha z^-_{\boldsymbol{n}}\boldsymbol{L}^-_{\boldsymbol{n}} >_{\partial E^{ae}} \\ =& -\int_{\partial E^{ae}} \left(\boldsymbol{W}_h\cdot\boldsymbol{L}^-_{\boldsymbol{n}}\right) z^-_{\boldsymbol{n}} \left(D_{11}^{ae}\boldsymbol{L}^-_{\boldsymbol{n}}\cdot\boldsymbol{U}_h + 2H_{1k}^{ae}\wp_{tens}(\boldsymbol{L}^{-'}_{\boldsymbol{n}',k}) : \wp_{tens}(\boldsymbol{\Psi}_{\boldsymbol{n}}(\boldsymbol{U}_h)\right) \\ &+ \int_{\partial E^{ae}} \left(\boldsymbol{W}_h\cdot\boldsymbol{L}^-_{\boldsymbol{n}}\right) z^-_{\boldsymbol{n}} \left(D_{11}^{ae}\boldsymbol{L}^-_{\boldsymbol{n}}\cdot\boldsymbol{\Pi}_{\boldsymbol{n}'}(\boldsymbol{U}'_h) + 2H_{1k}^{ae}\wp_{tens}(\boldsymbol{L}^{-'}_{\boldsymbol{n}',k}) : \wp_{tens}(\boldsymbol{U}'_h)\right) \end{aligned} \tag{55}$$

Then, we exchange the role of acoustic and elastic elements. Let us consider the elastic element, now denoted E. In this case, the same interface is consequently denoted ∂E^{ea} and the acoustic element E'. Taking into account (54) and (52), The flux term in (19) becomes:

$$\begin{aligned}
&< \boldsymbol{W}_h, \hat{\boldsymbol{F}}_{\boldsymbol{n}}(\boldsymbol{U}_h, \boldsymbol{U}'_h) - \boldsymbol{F}(\boldsymbol{U}_h) >_{\partial E^{ea}} \\
=&- < \boldsymbol{W}_h, \alpha_k z^-_{\boldsymbol{n},k} \boldsymbol{L}^-_{\boldsymbol{n},k} >_{\partial E^{ea}} \\
=&- \int_{\partial E^{ea}} \left(\boldsymbol{W}_h \cdot \boldsymbol{L}^-_{\boldsymbol{n},k} \right) z^-_{\boldsymbol{n},k} \left(2D^{ea}_{kl} \wp_{tens}(\boldsymbol{L}^-_{\boldsymbol{n},l})) : \wp_{tens}(\boldsymbol{U}_h) - H^{ea}_{k1} \boldsymbol{L}^{-'}_{\boldsymbol{n}'} \cdot \boldsymbol{\Pi}_{\boldsymbol{n}}(\boldsymbol{U}_h) \right) \\
&+ \int_{\partial E^{ea}} \left(\boldsymbol{W}_h \cdot \boldsymbol{L}^-_{\boldsymbol{n},k} \right) z^-_{\boldsymbol{n},k} \left(2D^{ea}_{kl} \wp_{tens}(\boldsymbol{L}^-_{\boldsymbol{n},l})) : \wp_{tens}(\boldsymbol{\Psi}_{\boldsymbol{n}'}(\boldsymbol{U}'_h)) - H^{ea}_{k1} \boldsymbol{L}^{-'}_{\boldsymbol{n}'} \cdot \boldsymbol{\Pi}_{\boldsymbol{n}}(\boldsymbol{U}'_h) \right)
\end{aligned} \tag{56}$$

In both cases, (55) and (56), when a FE discretization is applied, we obtained two flux matrices, one for E itself and the other coupling E with E'. We note that the two matrices $[R^{ae}]$ and $[R^{ea}]$ being analytically inverted, all terms in (55) and (56) are explicitly implemented, and the flux matrices are calculated once at the beginning of each dynamic calculation and stored. In other words, they are not calculated in each time step, so their computational cost is limited.

4. Validation of the upwind numerical fluxes

This section aims to validate the proposed upwind numerical fluxes, particularly on the acoustic/elastic interface, and demonstrate the performance of the coupled dG solver. For this purpose, a numerical/analytical comparison is carried out by considering an example with a circular acoustic/elastic interface for which analytical solutions are available [26].

We consider $\Omega = \Omega_1 \cup \Omega_2$, with Ω_1 a square fluid domain $[0, L_x] \times [0, L_y]$ with $L_x = L_y = 600$m, inside which there is a circular solid inclusion Ω_2 centered at $(x_0, y_0) = (330, 299)$m and with radius $a = 119$m (see Figure 3a). The acoustic wave speed in the fluid domain Ω_1 with a density of $\rho_1 = 1000 \frac{kg}{m^3}$ is $c = 1500$m/s, while the speeds of the pressure and shear waves in the solid domain Ω_2 with a density of $\rho_2 = 2600 \frac{kg}{m^3}$ are $c_p = 4000$m/s and $c_s = 2000$m/s respectively.

An external loading, a uniformly distributed pressure, is applied to the left side of Ω_1. Its time dependence is a sinusoid signal defined by the following function (Figure 3b):

$$f(t) = sin(\omega_c t) - \frac{1}{2} sin(2\omega_c t), \qquad t \in [0, 0.025\text{s}] \tag{57}$$

The frequency content of the signal is centered at 40Hz (Figure 3c), and a cutoff frequency $f_c = 150$Hz can be defined, which gives rise to the shortest involved wavelength $\lambda_{min} = \min\{c, c_p, c_s\}/f_c = 10$m. In this work, the non-reflecting boundary condition is handeled by using the same approach proposed by Käser *et al.* [6]. The main idea resides in the choice of the numerical fluxes, which keeps only the outgoing wave modes and forbids incoming modes.

Finite element meshes with the 4-node quadrilateral (Q4) elements are used in the present work. It is noteworthy that the element size h^E is chosen with respect to λ_{min}. Herein, four different element sizes are considered: $h^E_1 = 4$m, $h^E_2 = 2$m, $h^E_3 = 1$m and $h^E_4 = 0.5$m, which correspond respectively to 2.5, 5, 10, and 20 elements per shortest wavelength.

The total simulation time is chosen to be 0.3s so that the incident wavefront passes entirely through the circular inclusion. For the choice of time steps, in the present work, the time integration is performed by using the fourth-order Runge-Kutta iterative method, which is explicit and conditionally stable. Hence, it is necessary to respect the following stability condition [9]:

$$\Delta t \leq \frac{CFL}{2N_p + 1} \min_E \left\{ \frac{h^E}{c_{max}} \right\} \tag{58}$$

where N_p is the order of FE basis function and $N_p = 1$ with the use of the Q4 elements, h^E is the size of element E, c_{max} is the fastest wave speed in E, and CFL is the Courant-Friedrichs-Levy number. Our numerical experiences demonstrate that $CFL = 0.6$ guarantees the stability of our space DG solver.

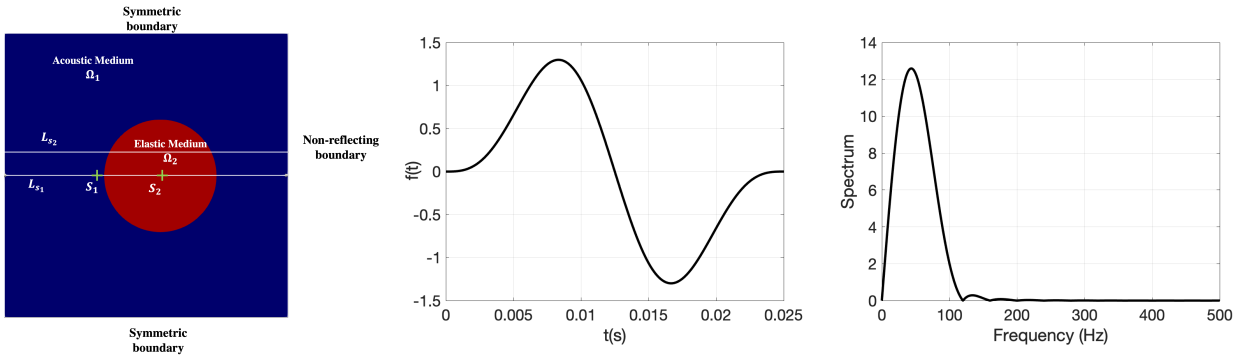

(a) (b) (c)

Figure 3. (a) Considered geometry with a circular acoustic/elastic interface and boundary conditions; (b) Initial sinusoid pulse placed over the left edge of the fluid medium, and (c) its frequency content

4.1. Convergence analysis and analytical/numerical comparison

First, a convergence analysis is performed using previously defined four different element sizes. Time signals in velocity, pressure, and stress are output and compared at two sampling points $S_1 = (200, 300)\text{m} \in \Omega_1$ and $S_2 = (330, 300)\text{m} \in \Omega_2$ (Figure 3a). Figure 4 shows that, for an element size less or equal to 2m, the convergence is reached as suggested by the negligible differences between the obtained signals.

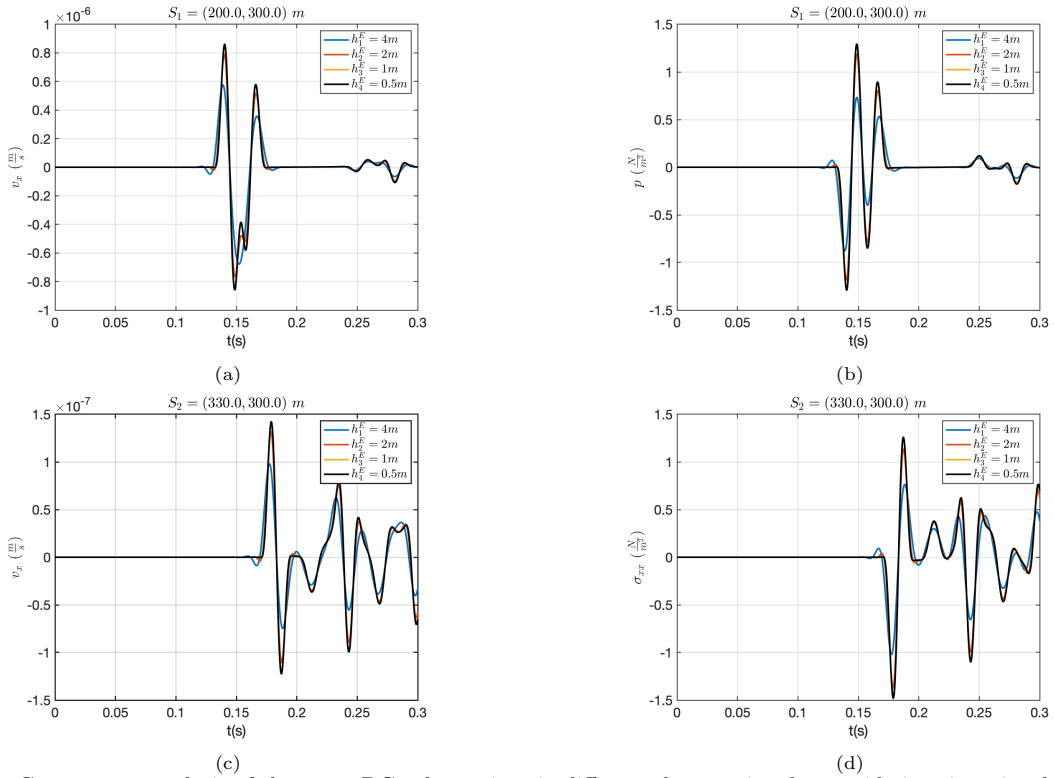

(a) (b) (c) (d)

Figure 4. Convergence analysis of the space DG solver using six different element sizes by considering time signals output at $S_1 = (200, 300)\text{m} \in \Omega_1$ and $S_2 = (330, 300)\text{m} \in \Omega_2$. (a) v_x at S_1; (b) p at S_1; (c) v_x at S_2; (d) σ_{xx} at S_2

Then, the wave propagation phenomena are analyzed. For the numerical simulation using $h_4^E = 0.5\text{m}$ and $\Delta t = 2.5\mu\text{s}$, three snapshots of the evolving longitudinal (pressure) and transverse (shear) wavefronts are displayed in Figure 5 by means of the Helmholtz decomposition. By this method, in the case of isotropic

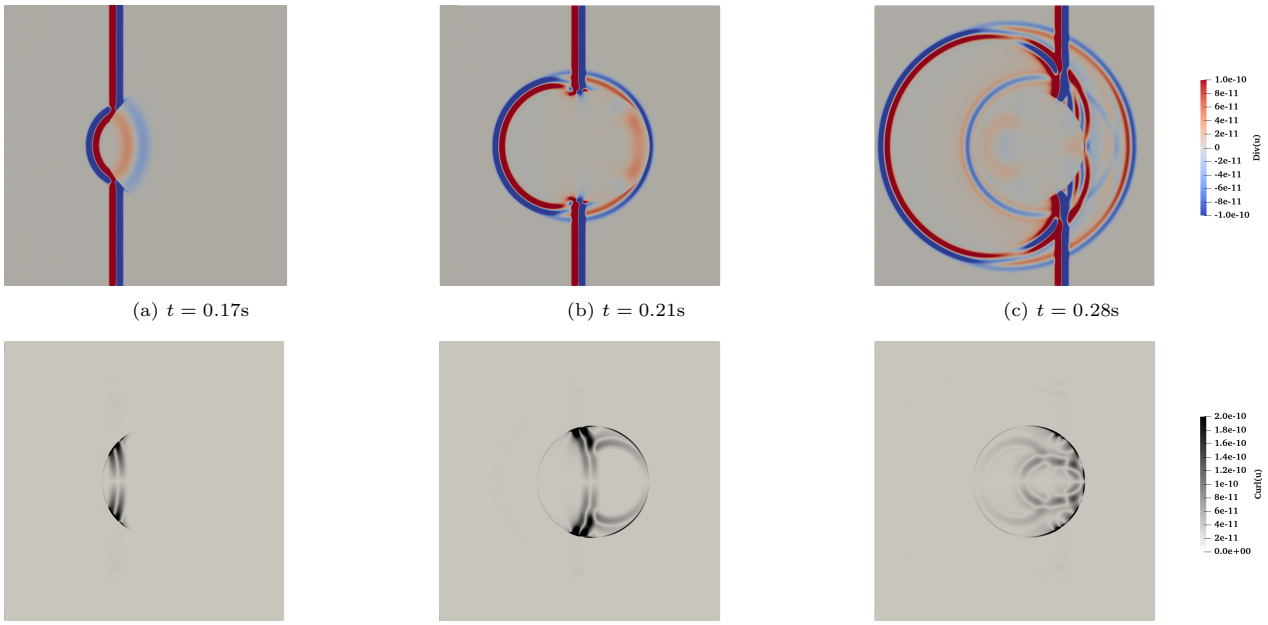

(a) $t = 0.17$s (b) $t = 0.21$s (c) $t = 0.28$s

(d) $t = 0.17$s (e) $t = 0.21$s (f) $t = 0.28$s

Figure 5. Wave propagation in the fluid-solid domain at different time instances; (a), (b) and (c): Longitudinal (pressure) wavefronts; (d), (e) and (f): Transverse (shear) wavefronts

and homogeneous elastic 2D medium, the scalar field $div(\boldsymbol{u})$ and the vector field $\boldsymbol{curl}(\boldsymbol{u})$ represent the longitudinal and transverse wavefronts, respectively. Expected wave phenomena are observed. The figures Figure 5(a-c) show the propagation of longitudinal waves in both media, which is faster in the solid inclusion, and wave reflection and transmission at the fluid-solid interface. Transverse waves are generated at the fluid-solid interface and only propagate inside the solid inclusion Ω_2 with a slower propagation speed than the longitudinal waves. Moreover, the minimum amplitude of the transverse waves is obtained along the horizontal diameter of the inclusion because no longitudinal to transverse wave conversion takes place due to the normal incidence of the incident wave at the fluid-solid interface (Figure 5(d-f)).

Finally, an analytical/numerical comparison is made using the analytical solution provided by Lombard et al. [26]. Figure 6 presents the comparison along the horizontal line $L_{s_1} = \{(x, y)|y = 300\text{m}\}$ and $L_{s_2} = \{(x, y)|y = 344\text{m}\}$ (Figure 3a) of the numerical stress and pressure fields obtained using $h_4^E = 0.5m$ and the corresponding analytical solution. Figure 6a shows the pressure field over the line L_s at $t = 0.1380s$, which is before the arrival of the wavefront at the acoustic/elastic interface. It is noteworthy that the points with $x \in [0, 211[\cup]449, 600]$for L_{s_1} lie in the acoustic medium and the points with $x \in]211, 449[$ are in the elastic medium. Hence, the y-axis in Figure 6(b-f) reports either the pressure p or the σ_{xx} component of the stress tensor, normalized by the maximum amplitude incident pressure p_{max}. It can be seen there is a good agreement between the numerical results and the analytical solution. In addition, Figure 7 shows the comparison on L_s of the numerical results of different element sizes with the analytical solution, which shows the convergence when the mesh gets finer.

Although visual comparison of the spatial signals shows that the proposed method and, in particular, the implemented numerical fluxes are working properly, these qualitative comparisons do not provide precise quantification and characterization of the differences between the results. Therefore, a more rigorous approach is presented in the next section to quantify the mismatch between the numerical and analytical solutions.

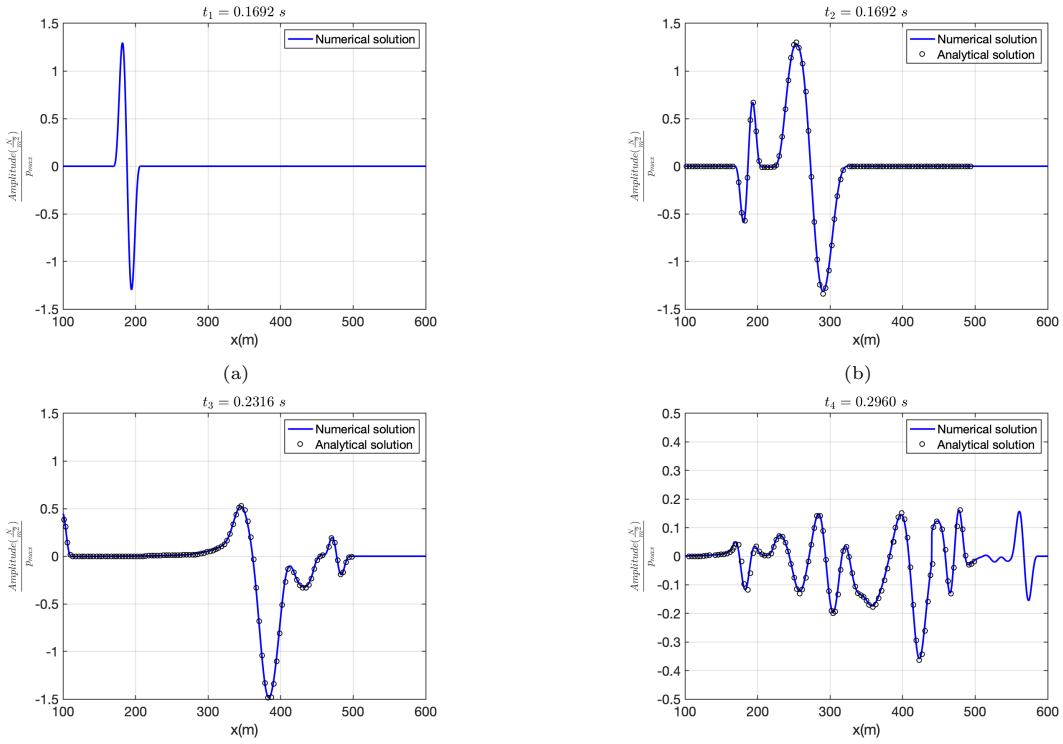

(a) (b)

(c) (d)

Figure 6. (a) Pressure wavefront in the acoustic medium Ω_1 before its interaction with the acoustic/elastic interface; (b)-(c) Numerical/analytical comparison along the horizontal line $L_{s_1} = \{(x, y)|y = 300\text{m}\}$; (d) Numerical/analytical comparison along the horizontal line $L_{s_2} = \{(x, y)|y = 344\text{m}\}$

;

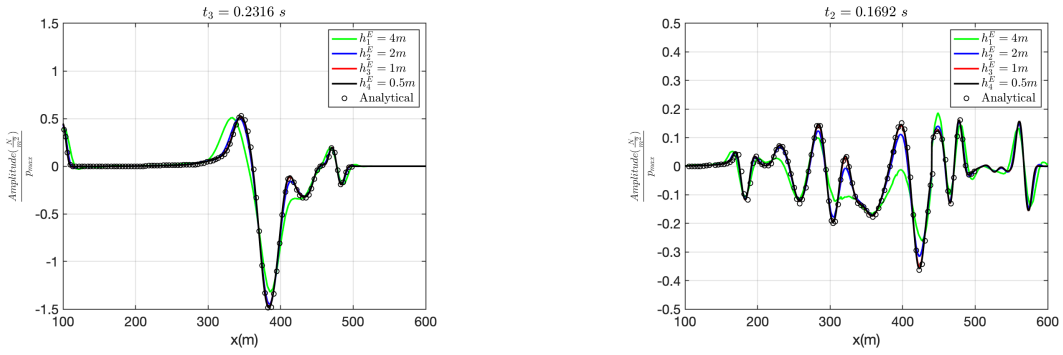

(a) (b)

Figure 7. (a) Numerical/analytical comparison along (a) L_{s_1} and (b) L_{s_2} for different element sizes

4.2. Space-Wavenumber misfit and goodness-of-fit criteria

Kristekova et al. proposed a criterion that quantifies and characterizes the misfit between two temporal signals using their time-frequency representations (TFR) [27, 28]. This criterion is shown to be able to detect envelope (or amplitude) and phase misfits and has a better performance compared to the standard Root-Mean-Squared (RMS) misfit criterion that overestimates the misfits up to 300% [27]. In the present work, we use a similar approach applied to spatial signals instead of temporal signals.

For this purpose, the Continuous Wavelet Transform (CWT) is used to obtain the space-wavenumber representation (SWR) of a 1-D spatial signal, denoted $g(x)$ below [27, 29]:

$$CWT(\xi,\ell)\{g\} = \frac{1}{\sqrt{\ell}}\int_{-\infty}^{+\infty} g(x)\psi^*\left(\frac{x-\xi}{\ell}\right)dx \tag{59}$$

where ξ is the translational parameter, ℓ is the scale parameter inversely proportional to wavenumber k, ψ is the analyzing wavelet (or basic wavelet), and $(\,\cdot\,)^*$ is the complex conjugate operator. Using ℓ, the analyzing wavelet is stretched in space at different scales.

Among plenty of signals that can be used as the analyzing wavelet, the Morlet wavelet is selected for the rest of the calculations in this work. It is an analytical signal whose spectrum has zero amplitudes at negative frequencies and is written as follows:

$$\psi(\eta) = \pi^{-1/4}e^{i\chi\eta-0.5\eta^2} \tag{60}$$

where χ is dimensionless wavenumber, and η is dimensionless space length. By choosing the appropriate ℓ and ξ, with a relation $k = \chi/\ell$ between the scale parameter ℓ and the wavenumber k, the SWR of the spatial signal $g(x)$ is defined as:

$$W(x,k)\{g\} = CWT(x,\frac{\chi}{k})\{g\} \tag{61}$$

The SWRs are obtained using the "cwt" function in MATLAB® with the parameter $\chi = 6$. Then a local SW envelope difference ΔE and a local SW phase difference ΔP with respect to a reference signal $g_{ref}(x)$ are defined for $g(x)$ as follows:

$$\Delta E(x,k) = |W(x,k)\{g\}| - |W(x,k)\{g_{ref}\}| \tag{62a}$$

$$\Delta P(x,k) = |W(x,k)\{g_{ref}\}|\frac{\mathrm{Arg}[W(x,k)\{g\}] - \mathrm{Arg}[W(x,k)\{g_{ref}\}]}{\pi} \tag{62b}$$

Afterward, local envelope and phase misfits, respectively called space-wavenumber envelope misfit (SWEM) and space-wavenumber phase misfit (SWPM), are defined as follows:

$$\mathrm{SWEM}(x,k) = \frac{\Delta E(x,k)}{\max_{(x',k')}(|W(x',k')\{g_{ref}\}|)}\ ,\ \mathrm{SWPM}(x,k) = \frac{\Delta P(x,k)}{\max_{(x',k')}(|W(x',k')\{g_{ref}\}|)} \tag{63}$$

Figure 8 presents the local envelope and phase misfits SWEM and SWPM of the spatial signals recorded on the previously defined line L_{s_1} and L_{s_2}. In each subfigure, the x-axis is the horizontal position of the points on the sampling line, the y-axis is the wavenumber, and the corresponding numerical signal and the analytical solution are also shown below the x-axis. It is noteworthy that the investigated wavenumber range is $k \in [0, 0.65]$ where the maximum wavenumber is obtained as $k_{max} = \frac{2\pi f_c}{c}$ in the acoustic domain. A general decreasing trend is observed in the local envelope and phase misfits as the element size is reduced. In addition, we note that the phase misfit is smaller than the envelope misfit for a given element size.

On the other hand, Figure 9 shows the envelope and phase misfits on L_s at different time instances for the finest element size of $h_4^E = 0.5m$. Similar to Figure 8, here again, the phase misfit is smaller compared to the envelope misfit at a given time. Moreover, both the envelope and phase misfit are bigger in the elastic domain compared to the acoustic domain. According to [28], a fit is considered as a "good" one if the envelope and phase misfits are less than 0.41 and 0.35, and an "excellent" one if the envelope and

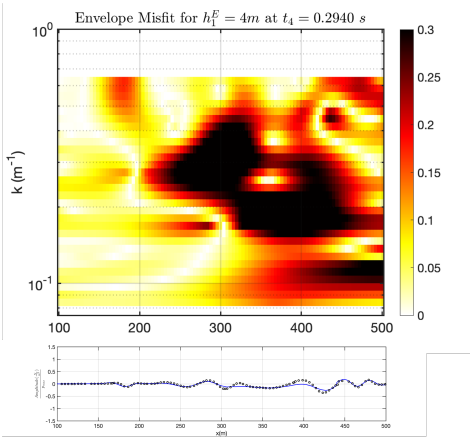

(a) SWEM for h_1^E

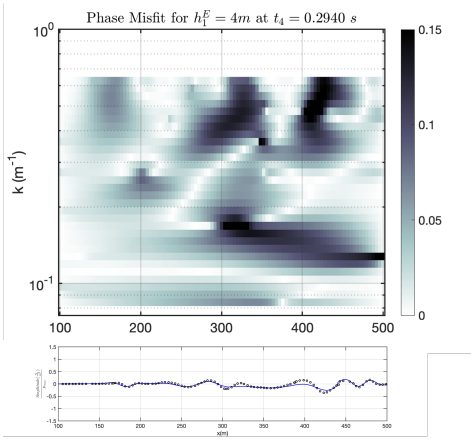

(b) SWPM for h_1^E

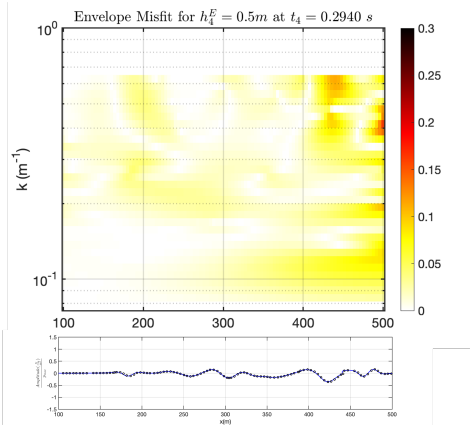

(c) SWEM for h_4^E

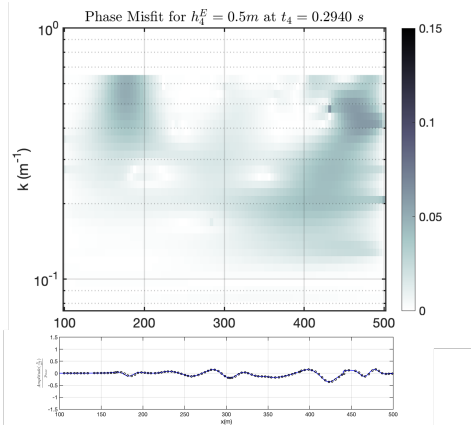

(d) SWPM for h_4^E

Figure 8. Space-wavenumber misfits between the numerical signal and the analytical solution on the sampling line L_{s_2} with different element sizes at $t_6 = 0.2940\ s$

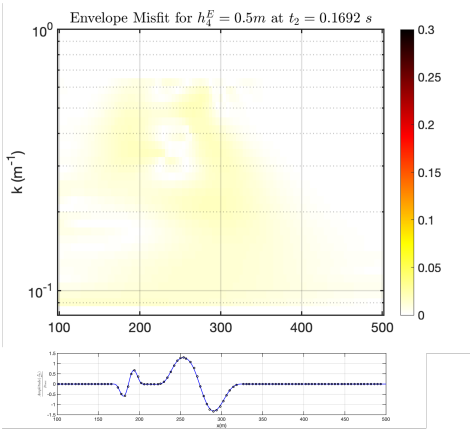

(a) SWEM at $t_2 = 0.1692$s

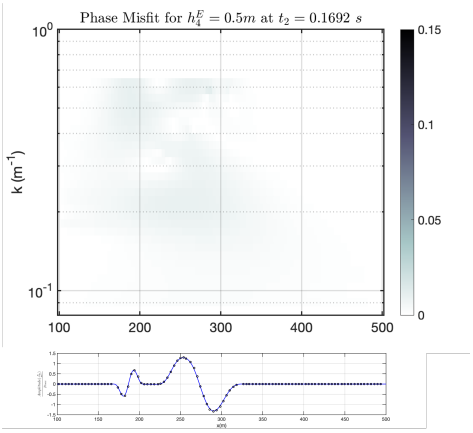

(b) SWPM at $t_2 = 0.1692$s

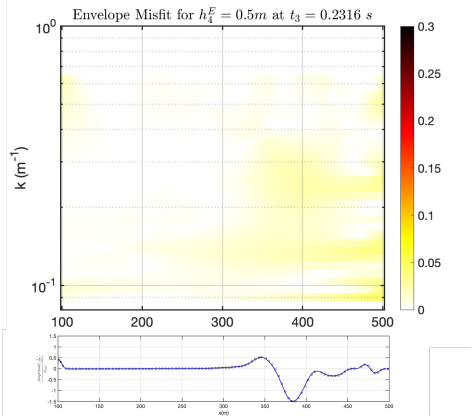

(c) SWEM at $t_3 = 0.2316$s

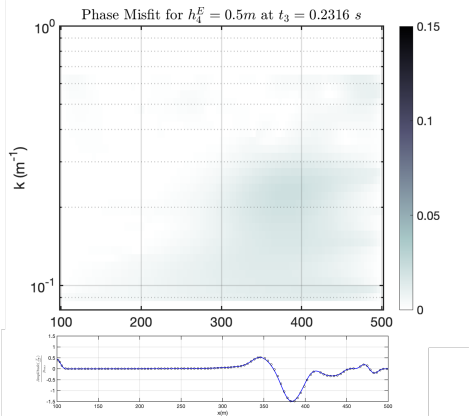

(d) SWPM at $t_3 = 0.2316$s

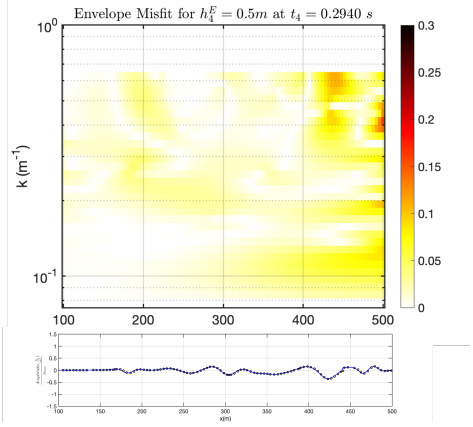

(e) SWEM at $t_4 = 0.2940$s

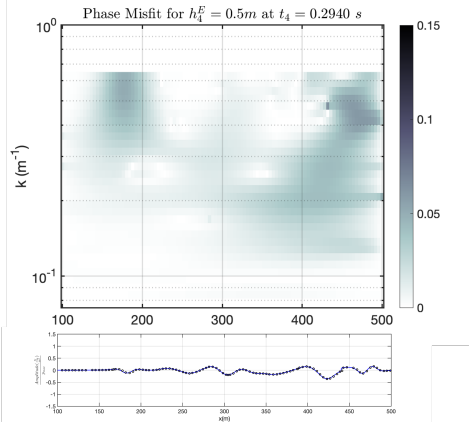

(f) SWPM at $t_4 = 0.2940$s

Figure 9. Space-wavenumber misfits between the numerical signal and the analytical solution on the sampling line L_{s_1} and L_{s_2} at different time instances for the element size $h_4^E = 0.5m$

phase misfits are less than 0.16 and 0.15, respectively. Based on this Goodness-of-Fit criterion, there is an excellent match between the numerical result and the analytical solution all over the sampling lines L_{s_1} and L_{s_2}, for the element sizes of $h_3^E = 1m$ and $h_4^E = 0.5m$.

Significant insights could have enriched this study if the analytical solutions over the entire domain was available to consider the L^2- or H^1- error norms. Nonetheless, obtaining the analytical solution over the entire domain has a high, even prohibitive, numerical cost.

5. Ultrasonic imaging of the simplified 3D-printed microstructure

The proposed coupled acoustic/elastic solver is used to simulate ultrasonic wave propagation in a 2D representation of a synthetic 3D-printed material microstructure that mimics the acoustic properties of biological tissues. The study aims to examine the influence of two key microstructure parameters, the area fraction and size of inclusion, on the resulting ultrasonic imaging.

For that purpose, as a printed microstructure, a rectangular domain made of a matrix with circular inclusions is considered (Figure 10a). Furthermore, the printed layer is assumed to be submerged in water, just as in the actual ultrasonic imaging process where tissues are usually surrounded by a fluid (blood or water). Hence, a water layer is added above and below the solid material layer (Figure 10a). The geometry size of the modeled domain is 6mm × 4.5mm, of which the thickness of each water layer is 1mm and the thickness of the 3D-printed material is 2.5mm. As depicted in Figure 10a, a non-reflecting boundary condition is applied to the sides and bottom edge of the rectangular geometry.

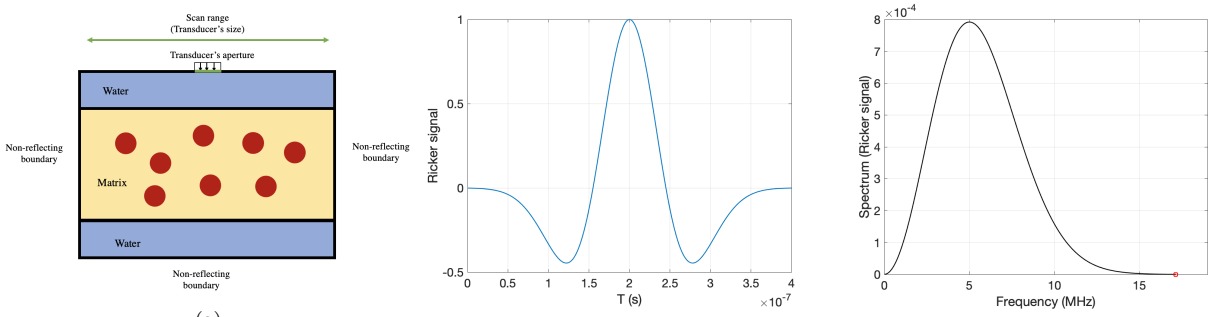

(a) (b) (c)

Figure 10. (a) 2D representative geometry of the studied 3D-printed microstructure embedded in water and boundary conditions; (b) Initial Ricker pulse generated by the transducer's piezoelectric element and (c) its frequency content

The ultrasonic wave is initiated in the domain with a simple sequential linear array transducer model. A sequential linear array transducer arranges multiple small piezoelectric elements along a straight line to produce 2D images. It works by transmitting on each element or group of elements (to increase the aperture size), receiving the echo information with the same element or group of elements, and reconstructing each line in the final 2D image displayed. To simplify the process, It is assumed that the aperture size is that of a single piezoelectric element. The operation of the transducer is performed sequentially; that is, after the first element has completed the transmit-receive procedure, the second element initiates the pulse and completes the same procedure, and so on, until the last element. Hence, the total length of the image is equivalent to the length of the transducer. The final image is composed of n different lines, with n corresponding to the total number of elements in the transducer.

In the examples presented in this paper, the transducer is assumed to have a length of 5.6mm and is composed of $n = 28$ piezoelectric elements, each with a size of 200µm. The vertical component of the velocity signal recorded on the transducer is used to perform the post-processing and to reconstruct the final image.

The ultrasonic pulse generated by the transducer is chosen to be a Ricker wavelet with the frequency content centered at $f_{max} = 5$MHz, and a cutoff frequency of $f_c = 17$MHz (Figure 10b and Figure 10c). The

Table I. Material properties of the quasi-incompressible matrix and the inclusions

Material	$\rho(kg/m^3)$	$\kappa(GPa)$	$\mu(MPa)$	$c_p(m/s)$	$c_s(m/s)$	$\lambda_p(\mu m)$	$\lambda_s(\mu m)$
water	1000	2.10	–	1500	–	$[215-500]$	–
matrix	1150	3.10	0.3	1620	17	$[230-540]$	$[2.4-5.6]$
inclusion	1200	6.78	1830	2680	1235	$[380-890]$	$[175-410]$

material properties and the range of ultrasonic wave wavelengths corresponding to the ultrasonic imaging frequency range considered here, $3-7$MHz, are presented in Table I.

One can observe that in the quasi-compressible matrix, the propagation speed of the shear wave is two orders of magnitude smaller than the one of the compression wave. Therefore, to capture the shear wave in the matrix, an unusually small element size is required, which makes the numerical simulation extremely computationally expensive. In addition, the shear wave generated at the matrix/inclusion interface propagates very slowly in the matrix and needs much more time to reach the transducer. As a result, we argue that its propagation in the matrix has a negligible impact on the velocity signal recorded by the transducer. Therefore, the finite element size in the numerical simulations is chosen based on the next shortest wavelength in the domain, the one determined by the shear wave in the inclusion. By selecting the element size of $h = 10\mu$m, we have respectively 10 and 18 elements per this shortest wavelength at the cutoff frequency 12.5MHz of the ricker signal and the maximum frequency 7MHz of the ultrasonic imaging frequency range considered in this work. The time step $\Delta t = 0.7\mu$s is calculated using (58) to ensure stability.

5.1. Advantages of modeling the quasi-incompressible material as an equivalent acoustic medium

In this section, the quasi-incompressible matrix in the composite is modeled using an equivalent acoustic material, i.e., both quasi-incompressible elastic material and acoustic material have the same compression wave speed (Table II). The objective is to see whether this modification impacts the velocity signal recorded on the transducer and evaluate the performance of the developed coupled acoustic/elastic solver compared to the pure elastic solver In this precise case. For this purpose, the layer of water is removed, and the transducer is placed directly in contact with the matrix over the entire top boundary (Figure 11a).

Table II. Material properties of the quasi-incompressible matrix, using acoustic and elastic models

Material	$\rho(kg/m^3)$	$\kappa(GPa)$	$\mu(MPa)$	$c_p(m/s)$	$c_s(m/s)$	$\lambda_p(\mu m)$	$\lambda_s(\mu m)$
matrix (acoustic)	1150	3.03	–	1620	–	$[230-540]$	–
matrix (elastic)	1150	3.10	0.3	1620	17	$[230-540]$	$[2.4-5.6]$

Figure 11b shows the vertical component of velocity recorded on the transducer using two different models, and there is an excellent agreement in the results. However, it was observed that by using the coupled solver, the total calculation time is decreased by 19%. The reason is that for the acoustic element in a 2D problem, we have 3 degrees of freedom per node (2 for velocity and 1 for pressure, while for the elastic problem, we have 5 degrees of freedom per node (2 for velocity and 3 for stress). Moreover, the size of the flux matrices on an acoustic/elastic interface is smaller than those on an elastic/elastic interface. Therefore the coupled acoustic/elastic is faster and less expensive in memory than the elastic solver. This advantage is more pronounced in 3D because, for 3D problems, we have for the acoustic case 4 degrees of freedom per node (3 for velocity and 1 for pressure), whereas for the elastic case 9 degrees of freedom per node (3 for velocity and 6 for stress). Hence, we chose to model the quasi-incompressible matrix by its equivalent acoustic medium for all the results presented below.

5.2. Reconstructed medical image: a multiparametric study

A B-mode image is a type of ultrasound image that displays the relative reflectivity of the target material. They are obtained by a simple post-processing procedure on the vertical component of the velocity signal

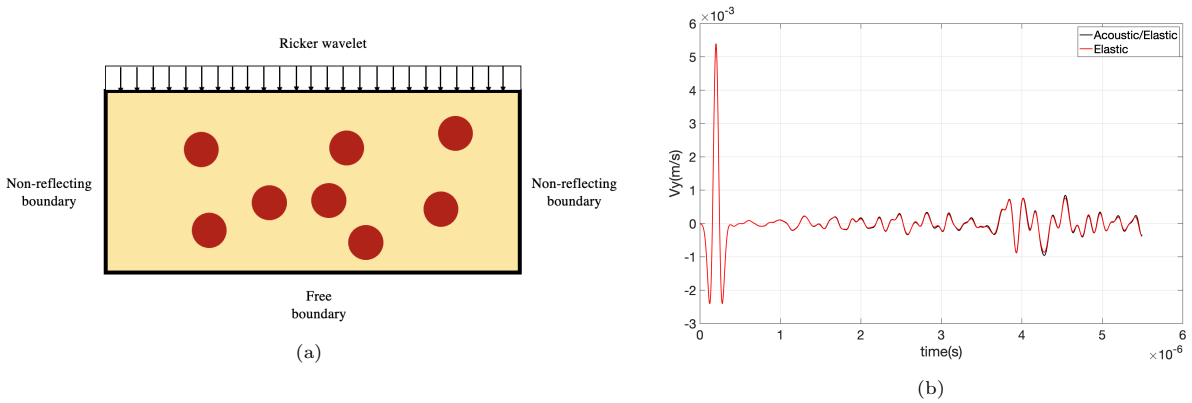

Figure 11. (a) Considered geometry and boundary conditions for comparing the elastic and acoustic model of the quasi-incompressible matrix, (b) Comparison of the vertical component of the velocity signal recorded on the transducer, obtained by coupled acoustic/elastic and pure elastic solver

recorded on the transducer. Indeed, the amplitude of the reflected echoes is used to generate an image, in which the brightness of each pixel representing the reflectivity of the object at that location (converted from time using an estimated effective propagation velocity of the medium). The image is typically displayed using a rectangular format, with parallel scan lines perpendicular to the direction of the ultrasound beam. The gray levels are represented by a 8-bit scale (0-255), with higher values corresponding to brighter pixels and lower values corresponding to darker pixels.

Here we investigate the impact of the area fraction (ϕ) and the diameter (D) of circular inclusions on the echogenicity of a single layer of 3D-printed composites (Figure 10a). For that purpose, the B-mode images are obtained for four different area fractions of inclusions: $\phi_1 = 1\%, \phi_2 = 3\%, \phi_3 = 5\%$ and $\phi_4 = 10\%$ and three different inclusion diameters $D_1 = 200\mu$m, $D_2 = 300\mu$m and $D_3 = 400\mu$m.

In the reconstruction of B-mode images, a series of post-processing steps are applied to the raw received signal from each piezoelectric element:

(1) Obtain the envelope of the received signal;
(2) Convert the amplitude to gray levels (G), with higher amplitudes resulting in brighter points;
(3) Convert the time to the distance of the reflector from the transducer by multiplying the time by the propagation speed of the compression wave in water, $c_{p,water} = 1500m/s$, and dividing by two. This is done to account for the wave traveling to the object and back to the transducer.

Figure 12 shows these steps applied to the raw signal obtained for a piezoelectric element for the case of $\phi = 10\%$ and $D = 200\mu$m. The final image is obtained by assembling all the gray level vectors, where the vertical axis shows the distance of the reflector from the transducer, and the lateral axis shows the total scan range, which in this paper is the size of the transducer.

As an example, Figure 13 depicts two different geometries and the corresponding B-mode images (all the numbers are in millimeters). One can observe that the water-matrix interface at the distance of 1mm is perfectly depicted. A horizontal dashed red line is also added to the B-mode image to show the ideal location of the matrix-water interface at the distance of 3.5mm. This interface might not be easily distinguishable in some cases, while it is very important if we want to obtain precisely the thickness of the imaged layer.

Figure 14 presents the reconstructed B-mode images for all the mentioned area fractions and sizes of inclusions. It can be observed that as the area fraction of the inclusion decreases, the matrix-water interface becomes more visible. However, the interface appears to be closer to the transducer than it actually is. This is because the post-processing steps assume the medium in which the wave is propagating is water and therefore calculate distances based on the speed of sound in water. Since the speed of sound in the matrix is faster than that of water, the wave travels faster in the matrix and appears thus closer to the transducer.

We also observe that as the area fraction of the inclusions increases and the size of the inclusion decreases, the echogenicity of the material to ultrasound waves improves. However, this makes it more challenging to

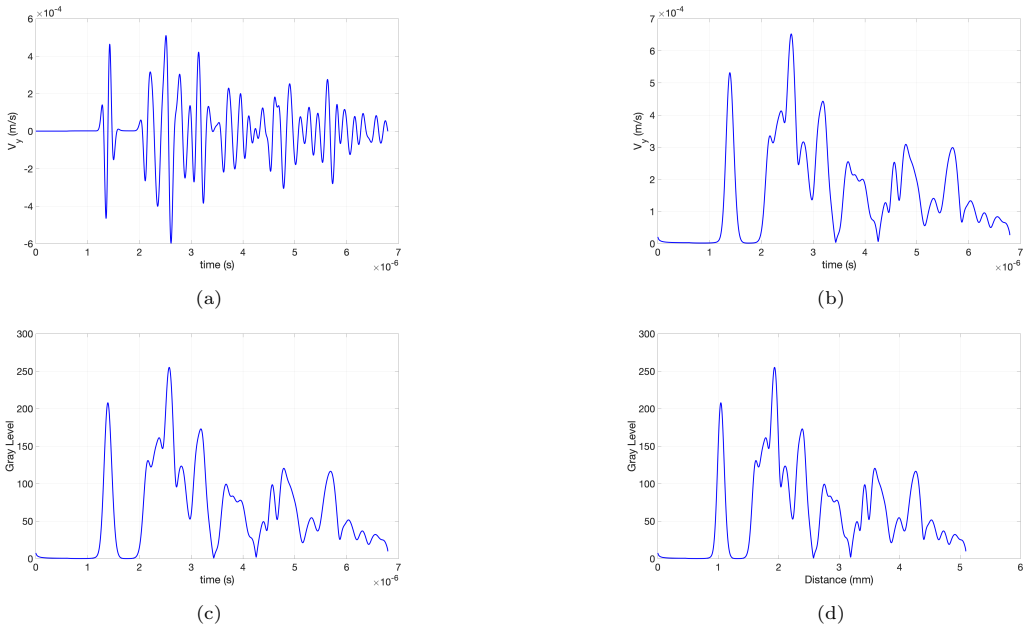

Figure 12. Post-processing steps for reconstruction of the B-mode medical image applied to a signal obtained for a single piezoelectric element for the case of $\phi = 10\%$ and $D = 200\mu$m (a) raw received signal, (b) extracted envelope, (c) converted to gray levels ranging from 0 to 255, and (d) time converted to distance of the reflector from the transducer.

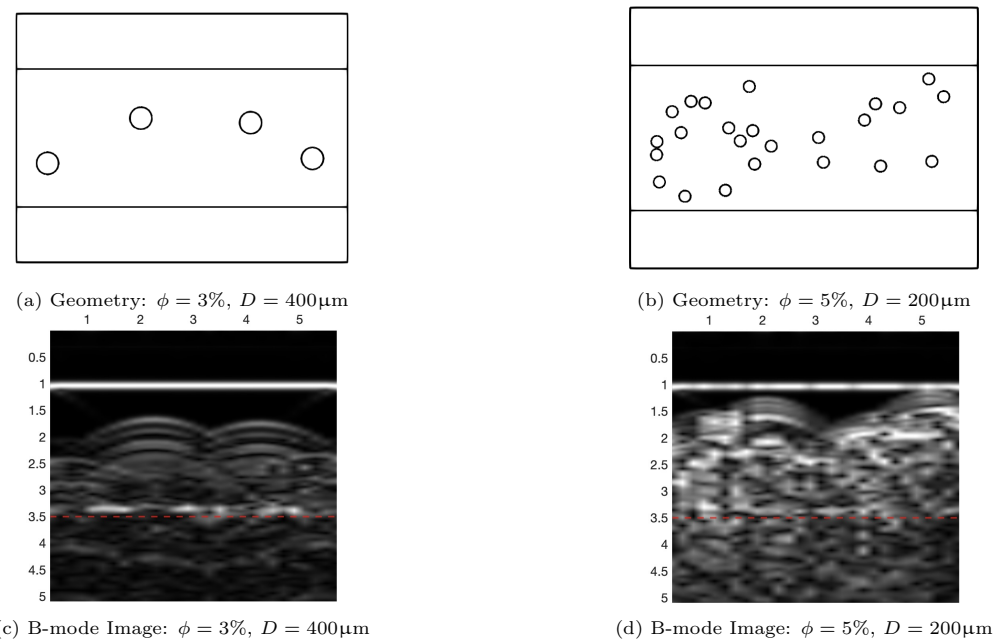

(a) Geometry: $\phi = 3\%$, $D = 400\mu$m

(b) Geometry: $\phi = 5\%$, $D = 200\mu$m

(c) B-mode Image: $\phi = 3\%$, $D = 400\mu$m

(d) B-mode Image: $\phi = 5\%$, $D = 200\mu$m

Figure 13. Two different configurations with various area fractions and diameter sizes of the inclusions, and corresponding B-mode images (all the sizes are in millimeters)

distinguish the matrix-water interface located at a distance of 3.5mm from the transducer. Therefore, it is challenging to see the actual thickness of the material, which is an important objective.

To have a more precise quantitative measure of echogenicity, the average gray level over the region

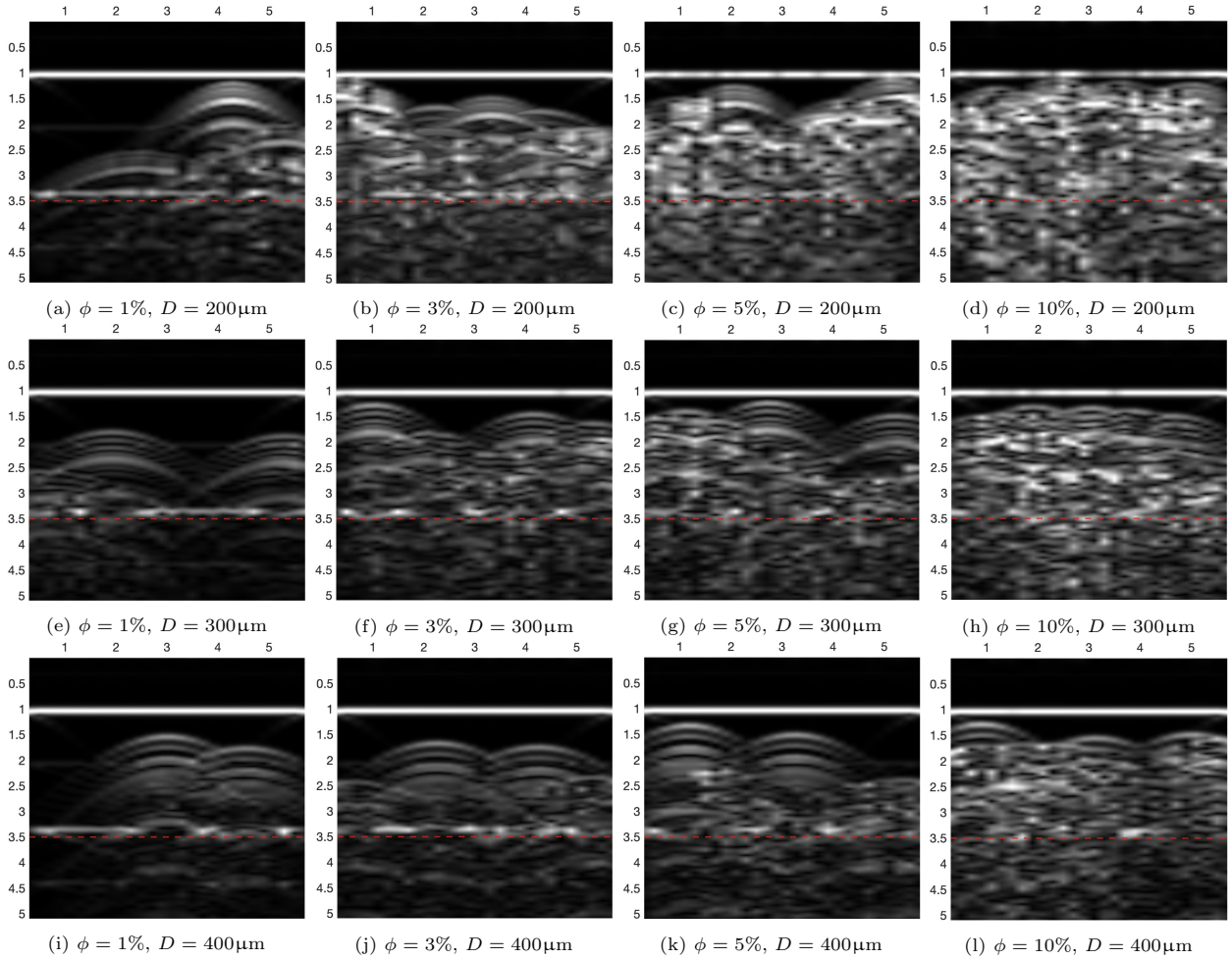

(a) $\phi = 1\%$, $D = 200\mu m$ (b) $\phi = 3\%$, $D = 200\mu m$ (c) $\phi = 5\%$, $D = 200\mu m$ (d) $\phi = 10\%$, $D = 200\mu m$

(e) $\phi = 1\%$, $D = 300\mu m$ (f) $\phi = 3\%$, $D = 300\mu m$ (g) $\phi = 5\%$, $D = 300\mu m$ (h) $\phi = 10\%$, $D = 300\mu m$

(i) $\phi = 1\%$, $D = 400\mu m$ (j) $\phi = 3\%$, $D = 400\mu m$ (k) $\phi = 5\%$, $D = 400\mu m$ (l) $\phi = 10\%$, $D = 400\mu m$

Figure 14. Reconstructed B-mode images for area fractions of inclusions 1%, 5%, 5%, and 10%

of interest (ROI), which corresponds to the actual thickness of the material, is chosen as a parameter to measure the reflectivity of the material to ultrasound waves, which is defined as follows:

$$\overline{G}_{ROI} = \frac{1}{N_{piezo} \times (d_{bottom} - d_{top})} \sum_{i=1}^{N_{piezo}} \int_{d_{top}}^{d_{bottom}} G(x_i, y) dy \tag{64}$$

where $d_{top} = 1$mm and $d_{bottom} = 3.5$mm are respectively the distance from the transducer to the top water-matrix interface and the bottom matrix-water interface. Moreover, the average gray level of the region below the bottom matrix-water interface, hereafter named the region of the residual signal (RORS), is calculated as follows:

$$\overline{G}_{RORS} = \frac{1}{N_{piezo} \times (d_{total} - d_{bottom})} \sum_{i=1}^{N_{piezo}} \int_{d_{bottom}}^{d_{total}} G(x_i, y) dy \tag{65}$$

where the total distance $d_{total} = T_{total} \times c_{p,water}/2$ which can be observed in Figure 12d. The ratio of $\overline{G}_{RORS}$ to $\overline{G}_{ROI}$ is used as another important metric to indicate how well the thickness of the material can be distinguished.

Figure 15a and Figure 15b show the average of the gray levels $\overline{G}_{ROI}$ with respect to the area fraction of the inclusions and the diameter size, respectively. These figures show an increasing trend in the average gray

level when the area fraction is increased for all three sizes. It also indicates that for a given area fraction of inclusion, the average gray level increases as the size of the inclusions decreases. However, the same behavior is observed for the $\overline{G}_{RORS}$ as illustrated in Figure 15c and Figure 15d, which is not desirable.

Looking at the ratio of the $\overline{G}_{RORS}$ to the $\overline{G}_{ROI}$, we notice that it increases for $D = 200\mu m$ and $D = 300\mu m$ as the area fraction is raised. On the other hand, for $D = 400\mu m$, the ratio decreases when we increase the area fraction from 5 to 10, which means that the actual thickness of the material is more recognizable. This behavior could be observed in Figure 15e and Figure 15f.

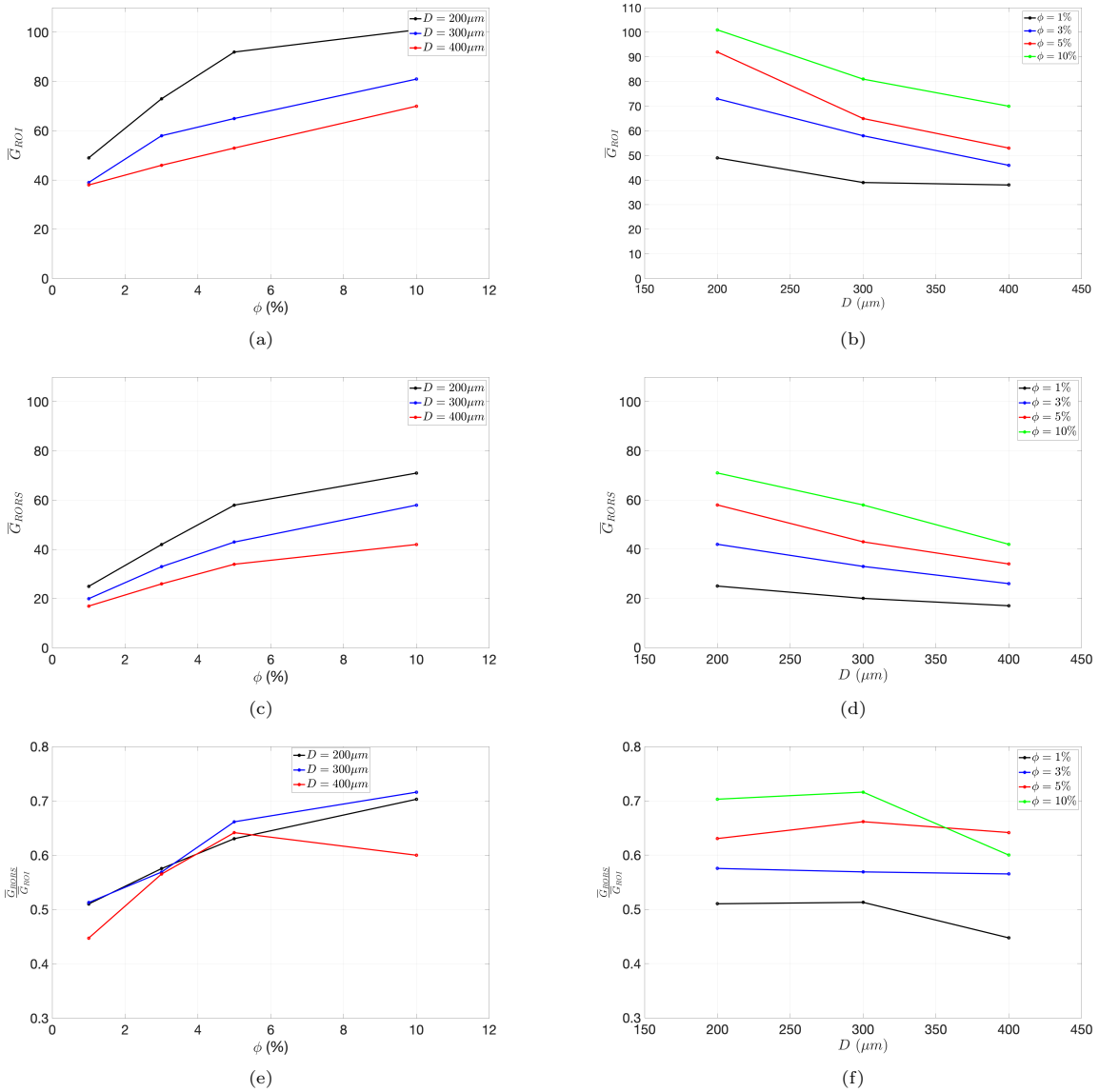

Figure 15. Quantitative analysis of the average gray levels. (a) $\overline{G}_{ROI}$, (c) $\overline{G}_{RORS}$, and (e) $\frac{\overline{G}_{RORS}}{\overline{G}_{ROI}}$ with respect to the area fraction ϕ; (b) $\overline{G}_{ROI}$, (d) $\overline{G}_{RORS}$, and (f) $\frac{\overline{G}_{RORS}}{\overline{G}_{ROI}}$ with respect to the inclusion's diameter D

The same calculations are repeated for another batch of samples with $\phi = 10\%$, and the results are presented in Table III. According to this table, the average gray levels are similar for two different batches, independent of the inclusions' distribution. However, a more rigorous statistical study is required to study

different random distributions of inclusions for a given area fraction and size of inclusions.

Table III. Comparison of average gray levels for two different batch of samples with $\phi = 10\%$

Diameter Size	$D = 200\mu$m		$D = 300\mu$m		400µm	
	1st batch	2nd batch	1st batch	2nd batch	1st batch	2nd batch
$\overline{G}_{ROI}$	101	100	81	81	70	73
$\overline{G}_{RORS}$	71	72	58	58	42	43
$\frac{\overline{G}_{RORS}}{\overline{G}_{ROI}}$	0.70	0.72	0.72	0.72	0.60	0.59

Conclusions

The derivation of the upwind numerical fluxes for the space discontinuous Galerkin finite element method was first proposed for the numerical modeling of the coupled acoustic/elastic wave propagation in multidimensional media with arbitrary anisotropic solid and acoustic fluid. The upwind numerical fluxes derived at the acoustic/elastic interfaces are original within the frameworks of the first-order velocity-pressure and the first-order velocity-stress formulation governing the domains composed of acoustic and elastic subdomains. Developed by analytically solving the Riemann problem, they were expressed in explicit closed forms presented within a compact and intrinsic tensorial framework. An analytical/numerical comparison was performed for a problem with a circular acoustic/elastic interface, and it was shown that the developed numerical fluxes provided accurate results. Indeed, according to local misfit criteria, which decompose the difference between two signals into the envelope (amplitude) and phase misfits, the mismatch between the numerical and analytical solutions was quantified, and numerical errors were evaluated. However, it is necessary to compare the performance of the proposed method to other methods, such as those developing the numerical flux (e.g., the penalty flux method), in terms of accuracy and convergence rate. This needs yet to be studied in detail in future works. Finally, the developed coupled solver was applied to simulate ultrasonic wave propagation in a simplified model of a 3D-printed matrix-inclusion composite microstructure intended to mimic the acoustic behavior of the biological tissues under the ultrasonic imaging procedure. A parametric study of the effects of the area fraction and the size of the inclusions on the average gray level of the reconstructed B-images was performed. It was shown that increasing the area fraction of the circular inclusions and decreasing their size improved the echogenicity of the 3D-printed composite layer. However, it also makes it more challenging to determine the thickness of the layer accurately. Modification of the microstructure is therefore necessary and should be investigated in future work.

Acknowledgments

The authors would like to thank Dr. Bruno Lombard (research director at LMA, Marseille, France) for kindly providing the analytical solution required for validating the numerical results. This work was granted by (Île-de-France Region, DIM Respore, Biomodex) Computations were performed using HPC resources from the "Mésocentre" computing center of CentraleSupélec and ENS Paris-Saclay.

CRediT authorship contribution statement

Hossein Kamalinia: Conceptualization, Software, Validation, Formal analysis, Writing - Original Draft, Writing - Review & Editing, Visualization. **Andrea Barbarulo:** Validation, Writing - Review & Editing, Funding acquisition. **Bing Tie:** Conceptualization, Methodology, Software, Validation, Writing - Original Draft, Writing - Review & Editing, Supervision, Funding acquisition.

References

[1] L. C. Wilcox, G. Stadler, C. Burstedde, O. Ghattas, A high-order discontinuous Galerkin method for wave propagation through coupled elastic–acoustic media, Journal of Computational Physics 229 (24) (2010) 9373–9396. doi:10.1016/j.jcp.2010.09.008.
URL https://linkinghub.elsevier.com/retrieve/pii/S0021999110005024

[2] L. Di Bartolo, R. R. Manhisse, C. Dors, Efficient acoustic-elastic FD coupling method for anisotropic media, Journal of Applied Geophysics 174 (2020) 103934. doi:10.1016/j.jappgeo.2019.103934.
URL https://linkinghub.elsevier.com/retrieve/pii/S0926985119303064

[3] D. Komatitsch, C. Barnes, J. Tromp, Wave propagation near a fluid-solid interface: A spectral-element approach, GEOPHYSICS 65 (2) (2000) 623–631. doi:10.1190/1.1444758.
URL https://library.seg.org/doi/10.1190/1.1444758

[4] D. Komatitsch, S. Tsuboi, J. Tromp, The spectral-element method in seismology, in: A. Levander, G. Nolet (Eds.), Geophysical Monograph Series, Vol. 157, American Geophysical Union, Washington, D. C., 2005, pp. 205–227. doi:10.1029/157GM13.
URL http://www.agu.org/books/gm/v157/157GM13/157GM13.shtml

[5] E. Chaljub, B. Valette, Spectral element modeling of three dimensional wave propagation in a self-gravitating Earth with an arbitrarily stratified outer core, Geophysical Journal International 158 (1) (2004) 131–141, arXiv: physics/0308102. doi:10.1111/j.1365-246X.2004.02267.x.
URL http://arxiv.org/abs/physics/0308102

[6] M. Käser, M. Dumbser, An arbitrary high-order discontinuous Galerkin method for elastic waves on unstructured meshes - I. The two-dimensional isotropic case with external source terms, Geophysical Journal International 166 (2) (2006) 855–877. doi:10.1111/j.1365-246X.2006.03051.x.
URL https://academic.oup.com/gji/article-lookup/doi/10.1111/j.1365-246X.2006.03051.x

[7] M. Dumbser, M. Käser, An arbitrary high-order discontinuous Galerkin method for elastic waves on unstructured meshes - II. The three-dimensional isotropic case, Geophysical Journal International 167 (1) (2006) 319–336. doi:10.1111/j.1365-246X.2006.03120.x.
URL https://academic.oup.com/gji/article-lookup/doi/10.1111/j.1365-246X.2006.03120.x

[8] J. de la Puente, M. Käser, M. Dumbser, H. Igel, An arbitrary high-order discontinuous Galerkin method for elastic waves on unstructured meshes - IV. Anisotropy, Geophysical Journal International 169 (3) (2007) 1210–1228. doi:10.1111/j.1365-246X.2007.03381.x.
URL https://academic.oup.com/gji/article-lookup/doi/10.1111/j.1365-246X.2007.03381.x

[9] B. Tie, A.-S. Mouronval, Systematic development of upwind numerical fluxes for the space discontinuous Galerkin method applied to elastic wave propagation in anisotropic and heterogeneous media with physical interfaces, Computer Methods in Applied Mechanics and Engineering 372 (2020) 113352. doi:10.1016/j.cma.2020.113352.
URL https://linkinghub.elsevier.com/retrieve/pii/S0045782520305375

[10] Q. Zhan, Q. Ren, M. Zhuang, Q. Sun, Q. H. Liu, An exact Riemann solver for wave propagation in arbitrary anisotropic elastic media with fluid coupling, Computer Methods in Applied Mechanics and Engineering 329 (2018) 24–39. doi:10.1016/j.cma.2017.09.007.
URL https://linkinghub.elsevier.com/retrieve/pii/S0045782517303559

[11] Q. Zhan, M. Zhuang, Y. Mao, Q. H. Liu, Unified Riemann solution for multi-physics coupling: Anisotropic poroelastic/elastic/fluid interfaces, Journal of Computational Physics 402 (2020) 108961. doi:10.1016/j.jcp.2019.108961.
URL https://linkinghub.elsevier.com/retrieve/pii/S0021999119306667

[12] T. Warburton, A Low-Storage Curvilinear Discontinuous Galerkin Method for Wave Problems, SIAM Journal on Scientific Computing 35 (4) (2013) A1987–A2012, publisher: Society for Industrial and Applied Mathematics. doi:10.1137/120899662.
URL https://epubs.siam.org/doi/10.1137/120899662

[13] R. Ye, M. V. de Hoop, C. L. Petrovitch, L. J. Pyrak-Nolte, L. C. Wilcox, A discontinuous Galerkin method with a modified penalty flux for the propagation and scattering of acousto-elastic waves, Geophysical Journal International 205 (2) (2016) 1267–1289. doi:10.1093/gji/ggw070.
URL https://academic.oup.com/gji/article-lookup/doi/10.1093/gji/ggw070

[14] J. Chan, Weight-adjusted discontinuous Galerkin methods: Matrix-valued weights and elastic wave propagation in heterogeneous media, International Journal for Numerical Methods in Engineering 113 (12) (2018) 1779–1809, _eprint: https://onlinelibrary.wiley.com/doi/pdf/10.1002/nme.5720. doi:10.1002/nme.5720.
URL https://onlinelibrary.wiley.com/doi/abs/10.1002/nme.5720

[15] K. Shukla, J. Chan, M. V. de Hoop, P. Jaiswal, A weight-adjusted discontinuous Galerkin method for the poroelastic wave equation: Penalty fluxes and micro-heterogeneities, Journal of Computational Physics 403 (2020) 109061. doi:10.1016/j.jcp.2019.109061.
URL https://www.sciencedirect.com/science/article/pii/S0021999119307661

[16] K. Guo, S. Acosta, J. Chan, A weight-adjusted discontinuous Galerkin method for wave propagation in coupled elastic-acoustic media, Journal of Computational Physics 418 (2020) 109632. doi:10.1016/j.jcp.2020.109632.
URL https://linkinghub.elsevier.com/retrieve/pii/S002199912030406X

[17] P. F. Antonietti, F. Bonaldi, I. Mazzieri, A high-order discontinuous Galerkin approach to the elasto-acoustic problem, Computer Methods in Applied Mechanics and Engineering 358 (2020) 112634. doi:10.1016/j.cma.2019.112634.
URL https://linkinghub.elsevier.com/retrieve/pii/S0045782519305183

[18] P. Antonietti, I. Mazzieri, High-order Discontinuous Galerkin methods for the elastodynamics equation on polygonal and polyhedral meshes, Computer Methods in Applied Mechanics and Engineering 342 (2018) 414–437. doi:10.1016/j.cma.2018.08.012.
URL https://linkinghub.elsevier.com/retrieve/pii/S0045782518303980
[19] B. Cockburn, G. E. Karniadakis, C.-W. Shu (Eds.), Discontinuous Galerkin Methods: Theory, Computation and Applications, Lecture Notes in Computational Science and Engineering, Springer-Verlag, Berlin Heidelberg, 2000. doi:10.1007/978-3-642-59721-3.
URL https://www.springer.com/gp/book/9783642640988
[20] R. J. LeVeque, Finite Volume Methods for Hyperbolic Problems, Cambridge Texts in Applied Mathematics, Cambridge University Press, Cambridge, 2002. doi:10.1017/CBO9780511791253.
URL https://www.cambridge.org/core/books/finite-volume-methods-for-hyperbolic-problems/97D5D1ACB1926DA1D4D52EAD6909E2B9
[21] B. Tie, A.-S. Mouronval, V. Nguyen, L. Series, D. Aubry, A unified variational framework for the space discontinuous Galerkin method for elastic wave propagation in anisotropic and piecewise homogeneous media, Computer Methods in Applied Mechanics and Engineering 338 (2018) 299–332. doi:10.1016/j.cma.2018.04.018.
URL http://www.sciencedirect.com/science/article/pii/S004578251631845X
[22] T. L. Poepping, H. N. Nikolov, M. L. Thorne, D. W. Holdsworth, A thin-walled carotid vessel phantom for Doppler ultrasound flow studies, Ultrasound in Medicine & Biology 30 (8) (2004) 1067–1078. doi:10.1016/j.ultrasmedbio.2004.06.003.
URL https://linkinghub.elsevier.com/retrieve/pii/S0301562904001541
[23] D. Hoang, D. Perrault, M. Stevanovic, A. Ghiassi, Surgical applications of three-dimensional printing: a review of the current literature & how to get started, Annals of Translational Medicine 4 (23) (2016) 456–456. doi:10.21037/atm.2016.12.18.
URL http://atm.amegroups.com/article/view/12912/13270
[24] J. R. Cook, R. R. Bouchard, S. Y. Emelianov, Tissue-mimicking phantoms for photoacoustic and ultrasonic imaging, Biomedical Optics Express 2 (11) (2011) 3193. doi:10.1364/BOE.2.003193.
URL https://www.osapublishing.org/boe/abstract.cfm?uri=boe-2-11-3193
[25] O. T. Von Ramm, S. W. Smith, Beam Steering with Linear Arrays, IEEE Transactions on Biomedical Engineering BME-30 (8) (1983) 438–452. doi:10.1109/TBME.1983.325149.
URL http://ieeexplore.ieee.org/document/4121676/
[26] B. Lombard, J. Piraux, Numerical treatment of two-dimensional interfaces for acoustic and elastic waves, Journal of Computational Physics 195 (1) (2004) 90–116. doi:10.1016/j.jcp.2003.09.024.
URL https://linkinghub.elsevier.com/retrieve/pii/S0021999103005126
[27] M. Kristekova, J. Kristek, P. Moczo, S. M. Day, Misfit Criteria for Quantitative Comparison of Seismograms, Bulletin of the Seismological Society of America 96 (5) (2006) 1836–1850. doi:10.1785/0120060012.
URL https://pubs.geoscienceworld.org/bssa/article/96/5/1836-1850/146655
[28] M. Kristeková, J. Kristek, P. Moczo, Time-frequency misfit and goodness-of-fit criteria for quantitative comparison of time signals, Geophysical Journal International 178 (2) (2009) 813–825. doi:10.1111/j.1365-246X.2009.04177.x.
URL https://academic.oup.com/gji/article-lookup/doi/10.1111/j.1365-246X.2009.04177.x
[29] A. Biswas, B. C. Si, Application of Continuous Wavelet Transform in Examining Soil Spatial Variation: A Review, Mathematical Geosciences 43 (3) (2011) 379–396. doi:10.1007/s11004-011-9318-9.
URL https://doi.org/10.1007/s11004-011-9318-9

Appendix A1: Acoustic-acoustic interface

By adding the three equations of (32), the unknown states $\{\boldsymbol{U}^a, \boldsymbol{U}^{a'}\}$ are eliminated and one obtains:

$$\boldsymbol{A}_{\boldsymbol{n}}(\boldsymbol{U}_h) - \alpha\lambda^-_{\boldsymbol{n}}\boldsymbol{M}(\boldsymbol{R}^-_{\boldsymbol{n}}) + \boldsymbol{A}'_{\boldsymbol{n}'}(\boldsymbol{U}'_h) - \alpha'\lambda^{-'}_{\boldsymbol{n}'}\boldsymbol{M}'(\boldsymbol{R}^{-'}_{\boldsymbol{n}'}) = \boldsymbol{0} \tag{66}$$

Regarding the definition of $\boldsymbol{M}$ (2), the Jacobian operator (4) and the eigenmodes (22) and (24), one can obtain the following equations by applying the $\boldsymbol{\wp}_{vect}$ and $\boldsymbol{\wp}_{scalar}$ on (66):

$$-p_h\boldsymbol{n} - p'_h\boldsymbol{n}' = \alpha z^-_{\boldsymbol{n}}\frac{1}{\sqrt{2}}\boldsymbol{n} + \alpha' z^{-'}_{\boldsymbol{n}'}\frac{1}{\sqrt{2}}\boldsymbol{n}' \tag{67a}$$

$$-\boldsymbol{n}\cdot\boldsymbol{v}_h - \boldsymbol{n}'\cdot\boldsymbol{v}'_h = -\frac{1}{\sqrt{2}}\alpha - \frac{1}{\sqrt{2}}\alpha' \tag{67b}$$

Hence, one obtains a linear system of two equations for two unknowns $\{\alpha, \alpha'\}$. Its solution gives rise to the expressions introduced in (34) by performing the following manipulations:

- To obtain α
  $-\frac{\overline{z_{\boldsymbol{n}}^-}^R}{z_{\boldsymbol{n}}^-}\frac{1}{\sqrt{2}}(\frac{\boldsymbol{n}'}{z_{\boldsymbol{n}'}^{-'}}\cdot \text{Eq.(67a)} + \text{Eq.(67b)})$ leads to:

$$\tilde{\boldsymbol{L}}_{\boldsymbol{n}}^- \cdot (\boldsymbol{U}_h - \boldsymbol{U}'_h) = \alpha \tag{68}$$

- To obtain α'
  $-\frac{\overline{z_{\boldsymbol{n}}^-}^R}{z_{\boldsymbol{n}'}^{-'}}\frac{1}{\sqrt{2}}(\frac{\boldsymbol{n}}{z_{\boldsymbol{n}}^-}\cdot \text{Eq.(67a)} + \text{Eq.(67b)})$ leads to:

$$\tilde{\boldsymbol{L}}_{\boldsymbol{n}'}^{-'} \cdot (\boldsymbol{U}'_h - \boldsymbol{U}_h) = \alpha' \tag{69}$$

Finally, using the (38b) and (68), the term in the variational formulation (19) and linked to the numerical flux on the acoustic-acoustic interface EE' is calculated as follows:

$$< \hat{\boldsymbol{F}}_{\boldsymbol{n}}(\boldsymbol{U}_h, \boldsymbol{U}'_h) - \boldsymbol{F}_{\boldsymbol{n}}(\boldsymbol{U}), \boldsymbol{W} >_{EE'} = < -\alpha z_n^- \boldsymbol{L}_n^-, \boldsymbol{W} >_{EE'} \tag{70a}$$

$$= z_n^- < -\tilde{\boldsymbol{L}}_n^- . \boldsymbol{U}_h, \boldsymbol{L}_n^- . \boldsymbol{W} >_{EE'} + z_n^- < \tilde{\boldsymbol{L}}_n^- . \boldsymbol{U}'_h, \boldsymbol{L}_n^- . \boldsymbol{W} >_{EE'} \tag{70b}$$

Appendix A2: Acoustic-elastic interface

In this appendix, we consider the numerical flux in an acoustic element E having an interface with an adjacent elastic element E'.

By applying the operator $\boldsymbol{\Pi}_{\boldsymbol{n}'}$ to (43c) and then adding it to the other two equations of (43), the unknown states $\{\boldsymbol{U}^a, \boldsymbol{U}^{c'}\}$ are eliminated and one obtains:

$$\boldsymbol{A}_{\boldsymbol{n}}(\boldsymbol{U}_h) - \alpha z_{\boldsymbol{n}}^- \boldsymbol{L}_{\boldsymbol{n}}^- + \boldsymbol{\Pi}_{\boldsymbol{n}'}(\boldsymbol{A}'_{\boldsymbol{n}'}(\boldsymbol{U}'_h)) - \alpha'_k z_{\boldsymbol{n}',k}^{-'} \boldsymbol{\Pi}_{\boldsymbol{n}'}(\boldsymbol{L}_{\boldsymbol{n}',k}^{-'}) = \boldsymbol{0} \tag{71}$$

Regarding the definition of the Jacobian operator by (4) and (16), the left eigenvectors by (24) and (26), one can obtain the following equations by applying the $\wp_{vect}$ and $\wp_{scalar}$ on (71):

$$-p_h \boldsymbol{n} - \boldsymbol{\sigma}'_h \cdot \boldsymbol{n}' = \alpha z_{\boldsymbol{n}}^- \frac{1}{\sqrt{2}} \boldsymbol{n} + \sum_l \alpha'_l z_{\boldsymbol{n}',l}^{-'} \frac{\boldsymbol{\gamma}'_{\boldsymbol{n}',l}}{\sqrt{2}} \tag{72a}$$

$$-\boldsymbol{n} \cdot \boldsymbol{v}_h - \boldsymbol{n}' \cdot \boldsymbol{v}'_h = -\alpha \frac{1}{\sqrt{2}} - \sum_l \alpha'_l (\boldsymbol{n}' \cdot \frac{\boldsymbol{\gamma}'_{\boldsymbol{n}',l}}{\sqrt{2}}) \tag{72b}$$

Hence, one obtains a linear system of four equations for four unknowns $\{\alpha, \{\alpha'_k\}\}$. Its solution gives rise to the expressions introduced in (44) by performing the following manipulations:

- First equation (for α):
  $\frac{1}{\sqrt{2}}(-\frac{\boldsymbol{n}}{z_{\boldsymbol{n}}^-}\cdot$ Eq.(72a) + Eq.(72b)) leads to:

$$\boldsymbol{L}_{\boldsymbol{n}}^- \cdot (\boldsymbol{U}_h - \boldsymbol{\Pi}_{\boldsymbol{n}'}(\boldsymbol{U}'_h)) = \alpha - \sum_l \frac{z_{\boldsymbol{n}}^- - z_{\boldsymbol{n}',l}^{-'}}{2 z_{\boldsymbol{n}}^-} (\boldsymbol{n} \cdot \boldsymbol{\gamma}'_{\boldsymbol{n}',l}) \alpha'_l \tag{73}$$

- Equations for $\{\alpha'_k\}$:
  For each k, $\sqrt{2}\frac{\boldsymbol{\gamma}'_{\boldsymbol{n}',k}}{z_{\boldsymbol{n}',k}^{-'}}\cdot$ (Eq.(72a)) leads to:

$$2\wp_{tens}(\boldsymbol{L}_{\boldsymbol{n}',k}^{-'}) : \wp_{tens}(\boldsymbol{U}'_h - \boldsymbol{\Psi}_{\boldsymbol{n}}(\boldsymbol{U}_h)) = \frac{z_{\boldsymbol{n}}^-}{z_{\boldsymbol{n}',k}^{-'}} \boldsymbol{n} \cdot \boldsymbol{\gamma}'_{\boldsymbol{n}',k} \alpha + \alpha'_k \tag{74}$$

In order to calculate the numerical flux on the acoustic-elastic interface for the acoustic element E, we recall that the equation (38b) is used. So, one needs to find α by solving the system of equations (44), which gives rise to:

$$\begin{pmatrix} \alpha \\ \{\alpha'_k\} \end{pmatrix} = [R^{ae}]^{-1} \cdot \begin{bmatrix} \boldsymbol{L}^-_{\boldsymbol{n}} \cdot (\boldsymbol{U}_h - \boldsymbol{\Pi}_{\boldsymbol{n}'}(\boldsymbol{U}'_h)) \\ \{2\wp_{tens}(\boldsymbol{L}^{-'}_{\boldsymbol{n}',k}) : \wp_{tens}(\boldsymbol{U}'_h - \boldsymbol{\Psi}_{\boldsymbol{n}}(\boldsymbol{U}_h))\} \end{bmatrix} \tag{75}$$

with $[R^{ae}]^{-1}$ defined by (48). (47) is finally proved.

Finally, the term in the variational formulation (19) for the acoustic element E and linked to the numerical flux on the acoustic-elastic interface EE' with the element E' is calculated using the following equation:

$$\begin{aligned} < \hat{\boldsymbol{F}}_{\boldsymbol{n}}(\boldsymbol{U}_h, \boldsymbol{U}'_h) - \boldsymbol{F}_{\boldsymbol{n}}(\boldsymbol{U}), \boldsymbol{W} >_{EE'} = & < -\alpha z^-_n \boldsymbol{L}^-_{\boldsymbol{n}}, \boldsymbol{W} >_{EE'} = -z^-_n < (D^{ae}_{11}\boldsymbol{L}^-_{\boldsymbol{n}}) \cdot (\boldsymbol{U}_h - \boldsymbol{\Pi}_{n'}(\boldsymbol{U}'_h)), \boldsymbol{L}^-_{\boldsymbol{n}} \cdot \boldsymbol{W} >_{EE'} \\ & + z^-_n < 2(H^{ae}_{1k}\wp_{tens}(\boldsymbol{L}^{-'}_{\boldsymbol{n}',k})) : \wp_{tens}(\boldsymbol{U}'_h - \boldsymbol{\Psi}_{\boldsymbol{n}}(\boldsymbol{U}_h)), \boldsymbol{L}^-_{\boldsymbol{n}} \cdot \boldsymbol{W} >_{EE'} \\ = & -z^-_n < (D^{ae}_{11}\boldsymbol{L}^-_{\boldsymbol{n}}) \cdot \boldsymbol{U}_h, \boldsymbol{L}^-_{\boldsymbol{n}} \cdot \boldsymbol{W} >_{EE'} + z^-_n < (D^{ae}_{11}\boldsymbol{L}^-_{\boldsymbol{n}}) \cdot \boldsymbol{\Pi}_{n'}(\boldsymbol{U}'_h), \boldsymbol{L}^-_{\boldsymbol{n}} \cdot \boldsymbol{W} >_{EE'} \\ + z^-_n < 2(H^{ae}_{1k}\wp_{tens}(\boldsymbol{L}^{-'}_{\boldsymbol{n}',k})) : \wp_{tens}(\boldsymbol{U}'_h), \boldsymbol{L}^-_{\boldsymbol{n}} \cdot \boldsymbol{W} >_{EE'} & - z^-_n < 2(H^{ae}_{1k}\wp_{tens}(\boldsymbol{L}^{-'}_{\boldsymbol{n}',k})) : \wp_{tens}(\boldsymbol{\Psi}_{\boldsymbol{n}}(\boldsymbol{U}_h)), \boldsymbol{L}^-_{\boldsymbol{n}} \cdot \boldsymbol{W} >_{EE'} \end{aligned} \tag{76}$$

Appendix A3: Elastic-acoustic interface

To calculate the numerical flux on the acoustic-elastic interface for the elastic element E, we recall that the equation (54) is used. So, one needs to find α_k by solving the system of equations (50), which gives rise to:

$$\begin{pmatrix} \{\alpha_k\} \\ \alpha' \end{pmatrix} = [R^{ea}]^{-1} \cdot \begin{bmatrix} \{2\wp_{tens}(\boldsymbol{L}^-_{\boldsymbol{n},k}) : \wp_{tens}(\boldsymbol{U}_h - \boldsymbol{\Psi}_{\boldsymbol{n}'}(\boldsymbol{U}'_h))\} \\ \boldsymbol{L}^{-'}_{\boldsymbol{n}'} \cdot (\boldsymbol{U}'_h - \boldsymbol{\Pi}_{\boldsymbol{n}}(\boldsymbol{U}_h)) \end{bmatrix} \tag{77}$$

with $[R^{ae}]^{-1}$ is defined in (53). Hence, (52) is proved.

Finally, the term in the variational formulation (19) for the elastic element E and linked to the numerical flux on the elastic-acoustic interface EE' with the element E' is calculated using the following equation:

$$\begin{aligned} < \hat{\boldsymbol{F}}_{\boldsymbol{n}}(\boldsymbol{U}_h, \boldsymbol{U}'_h) - \boldsymbol{F}_{\boldsymbol{n}}(\boldsymbol{U}), \boldsymbol{W} >_{EE'} = & < -\alpha_k z^-_{n,k} \boldsymbol{L}^-_{\boldsymbol{n},k}, \boldsymbol{W} >_{EE'} = z^-_{n,k} < H^{ea}_{k1}\boldsymbol{L}^{-'}_{\boldsymbol{n}'} \cdot (\boldsymbol{U}'_h - \boldsymbol{\Pi}_n(\boldsymbol{U}_h)), \boldsymbol{L}^-_{\boldsymbol{n},k} \cdot \boldsymbol{W} >_{EE'} \\ & + z^-_{n,k} < 2D^{ea}_{kl}\wp_{tens}(\boldsymbol{L}^-_{\boldsymbol{n},k}) : \wp_{tens}(\boldsymbol{U}_h - \boldsymbol{\Psi}_{\boldsymbol{n}}(\boldsymbol{U}'_h)), \boldsymbol{L}^-_{\boldsymbol{n},k} \cdot \boldsymbol{W} >_{EE'} \\ = & +z^-_{n,k} < H^{ea}_{k1}\boldsymbol{L}^{-'}_{\boldsymbol{n}'} \cdot \boldsymbol{U}'_h, \boldsymbol{L}^-_{\boldsymbol{n},k} \cdot \boldsymbol{W} >_{EE'} - z^-_{n,k} < H^{ea}_{k1}\boldsymbol{L}^{-'}_{\boldsymbol{n}'} \cdot \boldsymbol{\Pi}_n(\boldsymbol{U}_h), \boldsymbol{L}^-_{\boldsymbol{n}} \cdot \boldsymbol{W} >_{EE'} \\ -z_{n,k} < 2D^{ea}_{kl}\wp_{tens}(\boldsymbol{L}^-_{\boldsymbol{n},k}) : \wp_{tens}(\boldsymbol{U}_h), \boldsymbol{L}^-_{\boldsymbol{n},k} \cdot \boldsymbol{W} >_{EE'} & + z_{n,k} < 2D^{ea}_{kl}\wp_{tens}(\boldsymbol{L}^-_{\boldsymbol{n},k}) : \wp_{tens}(\boldsymbol{\Psi}_{\boldsymbol{n}'}(\boldsymbol{U}'_h)), \boldsymbol{L}^-_{\boldsymbol{n},k} \cdot \boldsymbol{W} >_{EE'} \end{aligned} \tag{78}$$

Appendix A4: Boundary Conditions Acoustic Solver

$$\hat{\boldsymbol{F}}_{\boldsymbol{n}}(\boldsymbol{U}_h, \boldsymbol{U}'_h) = \frac{1}{2}\big(\boldsymbol{A}_{\boldsymbol{n}}(\boldsymbol{U}_h) - \boldsymbol{A}'_{\boldsymbol{n}'}(\boldsymbol{U}'_h) - \alpha z^-_n \boldsymbol{L}^-_n + \alpha' z^{-'}_n \boldsymbol{L}^{-'}_n\big) \tag{79}$$

$$\hat{\boldsymbol{F}}_{\boldsymbol{n}}(\boldsymbol{U}_h, \boldsymbol{U}'_h) = \frac{1}{2}\begin{pmatrix} -(p_h + p'_h)\boldsymbol{n} \\ -(\boldsymbol{v}_h + \boldsymbol{v}'_h).\boldsymbol{n} \end{pmatrix} - \frac{1}{4}\begin{pmatrix} z^-_n \boldsymbol{n}.(\boldsymbol{v}_h - \boldsymbol{v}'_h)\boldsymbol{n} \\ \frac{1}{z^-_n}(p_h - p'_h) \end{pmatrix} \tag{80}$$

As for the numerical flux on an external element boundary, a neighbor element E' having the same acoustic behavior as E is introduced. In E' , it should be imposed that: $p'_h\boldsymbol{n} = 2\boldsymbol{g} - p_h\boldsymbol{n}$ and $\boldsymbol{v}'_h = \boldsymbol{v}_h$ for the

Neumann boundary conditions on $\partial\Omega_N$, and $p_h = p'_h$ and $\boldsymbol{v}'_h = 2\partial\boldsymbol{u}_D - \boldsymbol{v}_h$ for the Dirichlet boundary conditions on $\partial\Omega_D$.

For the Dirichlet boundary conditions, the flux is calculated as follows:

$$\hat{\boldsymbol{F}}_D = \hat{\boldsymbol{F}}_{\boldsymbol{n}}(\boldsymbol{U}_h, \boldsymbol{U}'_h) - \boldsymbol{F}_{\boldsymbol{n}}(\boldsymbol{U}) = \begin{pmatrix} \mathbf{0} \\ (v_h - v_D).\boldsymbol{n} \end{pmatrix} - \frac{1}{2}\begin{pmatrix} z_n^- \boldsymbol{n}.(v_h - v_D)\boldsymbol{n} \\ \mathbf{0} \end{pmatrix} \tag{81}$$

and for the Neumann boundary condition:

$$\hat{\boldsymbol{F}}_N = \hat{\boldsymbol{F}}_{\boldsymbol{n}}(\boldsymbol{U}_h, \boldsymbol{U}'_h) - \boldsymbol{F}_{\boldsymbol{n}}(\boldsymbol{U}) = \begin{pmatrix} p_h\boldsymbol{n} - \boldsymbol{g} \\ \mathbf{0} \end{pmatrix} - \frac{1}{2}\begin{pmatrix} \mathbf{0} \\ \frac{1}{z_n^-}(p_h - \boldsymbol{g}.\boldsymbol{n}) \end{pmatrix} \tag{82}$$

So the flux on the external boundaries where $\partial\Omega_{Ext} = \partial\Omega_D \cup \partial\Omega_N$ and $\partial\Omega_D \cup \partial\Omega_N = \phi$, is calulated as follows:

$$\begin{aligned} < \hat{\boldsymbol{F}}_{ext}, W >_{\partial\Omega} = < \hat{\boldsymbol{F}}_D, \boldsymbol{W} >_{\partial\Omega_D} + < \hat{\boldsymbol{F}}_N, \boldsymbol{W} >_{\partial\Omega_N} = & \frac{1}{2} < z_n^- \boldsymbol{n}.(\boldsymbol{v}_h)\boldsymbol{n}, \boldsymbol{w} >_{\partial\Omega_D} \\ & - \frac{1}{2} < z_n^- \boldsymbol{n}.(\boldsymbol{v}_D)\boldsymbol{n}, \boldsymbol{w} >_{\partial\Omega_D} + < \boldsymbol{n}.\boldsymbol{v}_h \ , \ q >_{\partial\Omega_D} - < \boldsymbol{n}.\boldsymbol{v}_D \ , \ q >_{\partial\Omega_D} \\ & + < p_h\boldsymbol{n}, \boldsymbol{w} >_{\partial\Omega_N} - < \boldsymbol{g}, \boldsymbol{w} >_{\partial\Omega_N} + \frac{1}{2} < \frac{1}{z_n^-} p_h, q >_{\partial\Omega_N} - \frac{1}{2} < \frac{1}{z_n^-}\boldsymbol{g}.\boldsymbol{n}, q >_{\partial\Omega_N} \end{aligned} \tag{83}$$